Segmentation of shallow slow slip events at the Hikurangi subduction zone explained by along-strike changes in the fault geometry and plate convergence rates

Andrea Perez-Silva[1], Yoshihiro Kaneko[2], Martha Kane Savage[1], Laura Wallace[3], Duo Li[4], and Charles A. Williams[3]

[1]Victoria University of Wellington
[2]Kyoto University
[3]GNS Science
[4]LMU Munich

November 23, 2022

Abstract

Over the last two decades, geodetic and seismic observations have revealed a spectrum of slow earthquakes along the Hikurangi subduction zone in New Zealand. Of those, shallow slow slip events (SSEs) that occur at depths of less than 15 km along the plate interface show a strong along-strike segmentation in their recurrence intervals, which vary from ~1 year from offshore Tolaga Bay in the northeast to ~5 years offshore Cape Turnagain ~300 km to the southeast. To understand the factors that control this segmentation, we conduct numerical simulations of SSEs incorporating laboratory-derived rate-and-state friction laws with both planar and non-planar fault geometries. We find that a relatively simple model assuming a realistic non-planar fault geometry can reproduce the characteristics of shallow SSEs as constrained by geodetic observations. Our preferred model captures the magnitudes and durations of SSEs, as well as the northward decrease of their recurrence intervals. Our results indicate that the segmentation of SSEs' recurrence intervals is favored by along-strike changes in both the plate convergence rate and the downdip width of the SSE source region. Modeled SSEs with longer recurrence interval concentrate in the southern part of the fault (offshore Cape Turnagain), where the plate convergence rate is lowest and the source region of SSEs is widest due to the shallower slab dip angle. Notably, the observed segmentation of shallow SSEs cannot be reproduced with a simple planar fault model, which indicates that a realistic plate interface is an important factor to account for in modeling SSEs.

Segmentation of shallow slow slip events at the Hikurangi subduction zone explained by along-strike changes in fault geometry and plate convergence rates

Andrea Perez-Silva[1], Yoshihiro Kaneko[2], Martha Savage[1], Laura Wallace[3,4], Duo Li[5], Charles Williams[3]

[1]School of Geography, Environment and Earth Sciences, Victoria University of Wellington, PO Box 600, Wellington 6140, New Zealand.

[2]Department of Geophysics, Kyoto University, Sakyo-ku, Kyoto 606-8501, Japan.

[3]GNS Science, PO Box 30368, Lower Hutt 5011, New Zealand.

[4]Institute for Geophysics, University of Texas at Austin, Austin, TX, USA.

[5]Department of Earth and Environmental Sciences, Ludwig-Maximilians-University Munich, Theresienstrasse 41, 80333 Munich, Germany.

Key Points:

- We simulate shallow slow slip events (SSEs) at Hikurangi margin using a rate-and-state fault model that incorporates 3D non-planar geometry.
- Model reproduces the magnitudes, duration and slip of shallow SSEs, as well as the along-strike change in their recurrence intervals.
- Along-strike changes in the fault geometry and the plate convergence rate may control the segmentation of shallow SSEs.

Corresponding author: Andrea Perez-Silva, `perezan@staff.vuw.ac.nz`

Abstract

Over the last two decades, geodetic and seismic observations have revealed a spectrum of slow earthquakes along the Hikurangi subduction zone in New Zealand. Of those, shallow slow slip events (SSEs) that occur at depths of less than 15 km along the plate interface show a strong along-strike segmentation in their recurrence intervals, which vary from ∼1 year from offshore Tolaga Bay in the northeast to ∼5 years offshore Cape Turnagain ∼300 km to the southeast. To understand the factors that control this segmentation, we conduct numerical simulations of SSEs incorporating laboratory-derived rate-and-state friction laws with both planar and non-planar fault geometries. We find that a relatively simple model assuming a realistic non-planar fault geometry can reproduce the characteristics of shallow SSEs as constrained by geodetic observations. Our preferred model captures the magnitudes and durations of SSEs, as well as the northward decrease of their recurrence intervals. Our results indicate that the segmentation of SSEs' recurrence intervals is favored by along-strike changes in both the plate convergence rate and the downdip width of the SSE source region. Modeled SSEs with longer recurrence interval concentrate in the southern part of the fault (offshore Cape Turnagain), where the plate convergence rate is lowest and the source region of SSEs is widest due to the shallower slab dip angle. Notably, the observed segmentation of shallow SSEs cannot be reproduced with a simple planar fault model, which indicates that a realistic plate interface is an important factor to account for in modeling SSEs.

Plain Language Summary

Slow slip events, with slower velocities and longer durations than regular earthquakes, have been detected at shallow depths (<15 km) along the Hikurangi subduction zone, where the Pacific Plate subducts beneath the North Island of New Zealand. The characteristics of these slow slip events change along the coast of the North Island, such that events occurring further south are less frequent (approximately every 5 years) than those further north (occurring at least once a year). To investigate the underlying causes of this change we undertake numerical simulations, which assume a realistic geometry of the subducting slab and incorporate the expected frictional behavior of fault rocks derived from laboratory experiments. Our model captures the main features of the observed slow slip events, such as their duration, slip, magnitude, as well as the observed changes in the frequency of slow slip. We find that this change is driven by variations in the rate of convergence between the tectonic plates, which increases northward along the Hikurangi subduction zone, and the width of the fault zone hosting the slow slip events. Less frequent slow slip events concentrate in the region where the plate convergence rate is lowest and the slow slip area is widest.

1 Introduction

Slow slip events (SSEs) are transient episodes of aseismic slip with longer durations and slower slip velocities than typical earthquakes. An SSE can generate millimeters to tens of centimeters of slip on a fault over periods of days to years (Schwartz & Rokosky, 2007). These events often occur at quasi-periodic intervals, spanning months to several years (Beroza & Ide, 2011), and play a significant role in the earthquake cycle where they occur, as they release part of the accumulated strain energy (e.g. Radiguet et al., 2012; Araki et al., 2017; Bartlow, 2020), and may influence the timing of earthquake occurrence (Kato et al., 2012; Ruiz et al., 2014; Kaneko et al., 2018). SSEs have been detected in various tectonic settings including strike-slip faults, (e.g. Linde et al., 1996; Wech et al., 2012; Wei et al., 2013; Rousset et al., 2019) and in volcanic islands (Cervelli et al., 2002; Segall et al., 2006; Brooks et al., 2006), however, they are most commonly observed in subduction zones (e.g. Lowry et al. (2001); Dragert et al. (2004); Obara et al. (2004); Hirose and Obara (2005); Ohta et al. (2006); Wallace and Beavan (2010); Outerbridge et al. (2010); Wei et al. (2012); Fu and Freymueller (2013); Dixon et al. (2014); Radiguet et al. (2016)).

The Hikurangi subduction zone, where the Pacific Plate subducts beneath the Australian plate (Figure 1a), is exceptional in the diversity of SSE characteristics that occur there (Wallace & Beavan, 2010). At Hikurangi, SSEs have been detected at both shallow and deep depths along the plate interface (Douglas et al., 2005; Wallace & Beavan, 2010; Wallace et al., 2012a; Wallace, 2020). Deep SSEs ($<$ 50 km depth) have been observed in the Kapiti and Manawatu regions, as well as in the Kaimanawa ranges (Figure 1a); whereas shallow SSEs ($<$ 15 km depth) concentrate along the east coast of the North Island, from offshore East Cape to offshore Cape Turnagain (Figure 1a). Deep and shallow SSEs exhibit contrasting source properties. Deep SSEs typically last 1 to 2 years, reach magnitudes larger than $\sim$ M_w7.0 and recur every $\sim$5 years (Wallace & Beavan, 2010; Wallace et al., 2012a; Bartlow et al., 2014; Ikari et al., 2020). In contrast, shallow SSEs have shorter durations (1 to 4 weeks), lower magnitudes (M_w6.0 - M_w6.6; Ikari et al., 2020) and their recurrence intervals range from $\sim$1 to 5 years (Douglas et al., 2005; Wallace & Beavan, 2010; Wallace et al., 2012a). For both deep and shallow Hikurangi SSEs, slip on the plate boundary can be centimetres to tens of centimetres.

Shallow SSEs along the Hikurangi margin display a marked along-strike segmentation in their recurrence interval, which increases southward along the strike of the margin (Wallace & Beavan, 2010; Wallace et al., 2012a; Wallace, 2020). In the northern part of the margin, offshore Tolaga Bay, SSEs recur more frequently, with 1-2 events detected each year. In the central part, offshore Gisborne and Hawke's Bay regions, the recurrence time is $\sim$1-2 years, whereas in the south, offshore Porangahau and Cape Turnagain, they occur every $\sim$5 years. Figure 1b illustrates the along-strike change in the recurrence interval along the margin. Similarly, along-strike changes in the recurrence interval of SSEs have been reported in other subduction zones, such as Alaska (Wei et al., 2012; Fu et al., 2015; H. Li et al., 2018), Cascadia (Brudzinski & Allen, 2007), Nankai (Obara, 2010; Takagi et al., 2019) and Mexico (Graham et al., 2016). We note that along-strike segmentation of deep SSEs at Hikurangi is not as well constrained as for shallow SSEs.

Several factors have been proposed to explain SSE segmentation based on modeling, and geodetic and seismic observations. Numerical simulations indicate that along-strike changes in effective normal stress (the difference between lithostatic load and pore fluid pressure) could lead to segmentation of SSEs' recurrence interval, with shorter intervals associated with lower effective normal stress (Liu, 2014; H. Li et al., 2018). Another model suggests that changes in the plate convergence rate and the width of the source region of SSEs may also affect the periodicity of these events (Shibazaki et al., 2012). Simulations of SSE cycles assuming a realistic plate geometry showed links between spatial variations in the plate dip and strike angles, and the segmentation of SSEs (D. Li & Liu, 2016). In addition, geodetic observations showed correlations between the location of locked asperities in the updip area with the segmentation of SSE recurrence interval and cumulative slip (Takagi et al., 2019). Other potential causes of SSE segmentation include spatial variations in pore fluid pressure due to silica enrichment (Audet & Bürgmann, 2014), and along-strike changes in the density of geological terranes in the overriding plate (Brudzinski & Allen, 2007; D. Li & Liu, 2017). A review of the factors that may affect the segmentation of SSEs can be found in H. Li et al. (2018). Yet it is still uncertain which of these factors control the segmentation of shallow SSEs along the Hikurangi margin.

In this study, we conduct numerical simulations to understand the factors that control the segmentation of shallow SSEs in Hikurangi. Our modelling approach accounts for continuum elasticity and a realistic 3D geometry of the plate interface, where the fault resistance to sliding is described by laboratory-derived rate-and-state friction laws. We note that while Shibazaki et al. (2019) modeled both shallow and deep SSEs and focused on their interactions with large earthquakes using a similar approach, the cause of the segmentation of shallow SSEs was not investigated. This paper is structured as follows. Section 2 introduces the method and parameter setup of our numerical model. In Section 3, we conduct a parameter exploration and describe a preferred model that best reproduces the observed characteristics of shallow SSEs. In Section 4, we discuss the factors that control the along-strike segmentation of shallow SSEs and the implications for other relevant observations.

[Figure 1 about here.]

2 Model setup

To simulate SSE cycles, we use the numerical code developed by D. Li and Liu (2016). There are three main ingredients of this computational approach: (1) it implements a quasi-dynamic formulation as defined by Rice (1993), (2) the fault constitutive response is given by rate-and-state friction laws with the aging form of state-variable evolution (Dieterich, 1979), and (3) it enables the incorporation of a 3D non-planar fault geometry. We describe the governing equations of the model in the supporting information (Text S1).

In the rate-and-state friction formulation, the evolution of the steady-state friction coefficient in response to a step change in slip velocity depends on the lab-derived friction parameters a and b (Dieterich, 1979; Blanpied et al., 1998). Materials with $a-b > 0$ are velocity-strengthening (VS), such that an increase in slip velocity results in an increase in steady-state friction, thus stabilizing slip. Materials with $a-b < 0$ are velocity-weakening (VW); increasing the slip velocity causes a decrease in steady-state friction, and slip can be unstable (seismic) or conditionally stable (Scholz, 1998).

The slip behavior of the fault largely depends on the effective fault stiffness ratio W/h^* (Liu & Rice, 2007; Barbot, 2019), where W is the downdip width of the VW region and h^* is the critical patch size to generate unstable slip (Rubin & Ampuero, 2005). If $W/h^* >> 1$ unstable slip may occur, while much smaller values point to stable slip (Liu & Rice, 2007). Previous numerical models (Liu & Rice, 2007, 2009; D. Li & Liu, 2016) have found that a W/h^* close to unity favors episodic slow slip behavior. This nondimensional ratio depends on the Poisson's ratio (ν), shear modulus (μ), effective normal stress ($\bar{\sigma}_n$), rate-and-state parameters (d_c and $a-b$) and fault geometry (equation

4 in Text S1). In addition to W/h^*, the ratio a/b has also been shown to control the fault slip behavior (Rubin, 2008; Barbot, 2019).

[Figure 2 about here.]

2.1 Fault geometry

The model assumes a 3D fault geometry of the Hikurangi plate interface based on Williams et al. (2013), which was constrained by earthquake locations and seismic reflection images. Our model fault extends 500 km along the Hikurangi margin (latitudes 41° S to 37° S) and covers the depth range from the trench, at 2.5 km depth below sea level, down to 30 km (Figure S1). We discretize the slab surface by 84906 triangular elements using Cubit/Trelis Software (`https://www.coreform.com/`) with each triangular element having an area of $\sim$1 km^2. Given that the smallest value of the critical nucleation size (h^*) is 80 km, $h^*/dx \sim 80$, where dx is the average length of the triangle edges (1 km). Such discretization ensures that h^* is well resolved, and is similar to that used in previous 3D simulations of SSEs (D. Li & Liu, 2016, 2017; H. Li et al., 2018; Perez-Silva et al., 2021).

2.2 Model parameters

To account for the shallow depths of SSEs, we set the shear modulus to 15 GPa, which is slightly above but comparable to the recently inferred range (6-14 GPa) at central Hikurangi using full waveform inversion of controlled-source seismic data (Arnulf et al., 2021). We assume a Poisson ratio of 0.25, corresponding to a Poisson solid.

The fault is loaded by spatially non-uniform plate motion. We set the plate convergence rate perpendicular to the trench and increasing linearly northwards from 36 to 60 mm/yr along the strike of the fault (red arrows in Figure 2a; see also Figure S1), which is consistent with the estimation from modeling of the campaign GPS velocity field (Wallace et al., 2004, 2012b). Slip partitioning occurs at the Hikurangi subduction margin, whereby the margin-parallel component of plate motion is accommodated by strike-slip faulting and tectonic-block rotation of the eastern North Island, and the shallow plate interface is dominated by trench-normal convergence (Wallace et al., 2004, 2009).

We define the the distribution of the friction parameters $(a - b)$ along the fault dip such that the VW region roughly matches with the along-dip extent of observed shallow SSEs (Figure 1a). Figure 2a shows the map view of the $(a-b)$ distribution. We set a uniform value of $(a-b)_{\mathrm{vw}} = -0.003$ or -0.0003 from 4 km depth until the downdip limit of the slip contours of shallow SSEs. The assumed $(a-b)_{\mathrm{vw}}$ are comparable to those obtained from friction experiments on incoming sediments to Hikurangi margin, where it ranges from -0.0004 to -0.0015 (Rabinowitz et al., 2018) and from -0.0019 to -0.003 (Ikari et al., 2020). VS conditions $(a - b > 0)$ are assumed outside of the VW region.

Low effective normal stress, or equivalently, high pore fluid pressures, have been adopted by several numerical models to reproduce SSEs' properties (e.g. Liu & Rice, 2007; Shibazaki & Shimamoto, 2007; Liu & Rice, 2009; Matsuzawa et al., 2010; Shibazaki et al., 2012; Matsuzawa et al., 2013; Liu, 2014; D. Li & Liu, 2016, 2017; H. Li et al., 2018; Wei et al., 2018; Shibazaki et al., 2019). This assumption is based on inferred high pore pressure conditions in the source regions of SSEs (Kodaira et al., 2004; Audet et al., 2009; Song et al., 2009; Audet & Kim, 2016), and it is also supported by geophysical observations at Hikurangi (Heise et al., 2013, 2017; Bassett et al., 2014; Eberhart-Phillips & Bannister, 2015; Eberhart-Phillips et al., 2017). Following this assumption, the effective normal stress $(\bar{\sigma}_n)$ is set to a low value ($\bar{\sigma}_n = 1$ or 10 MPa) in the VW region (Figure 2b). For simplicity, we do not assume along-dip changes in $\bar{\sigma}_n$ within this region.

We refer to the region with low $\bar{\sigma}_n$ and VW conditions as the *SSE zone*. Farther downdip of the SSE zone, $\bar{\sigma}_n = 50$ MPa (Figure 2b). From the trench (at 2.5 km depth) down to 4 km depth, $\bar{\sigma}_n$ increases from 7 to 30 MPa (Figure 2b). Since the updip extent of SSEs is not well constrained by observations, this assumption is set to avoid SSEs propagating all the way to the trench. To test the viability of this assumption, we additionally consider a case with low $\bar{\sigma}_n$ starting from the trench (Section 3.2.5).

The characteristic slip distance d_c is set to scale with $\bar{\sigma}_n$ and $(a-b)$ on the fault (equation 4 in Text S1) until it reaches 2 m, after which it remains constant. The increase of d_c with depth outside the SSE zone is motivated by computational efficiency (Lapusta et al., 2000) and produces the same results for shallow SSEs as using a constant d_c for all depths.

As the Hikurangi plate interface is estimated to be strongly coupled in the southern part of the margin (Wallace & Beavan, 2010), we set VW conditions ($a-b < 0$) and $\bar{\sigma}_n = 50$ MPa for $0 <$ Y < 50 km (Figure 2a and 2b, respectively). This parameter setting is not equivalent to a kinematic, fully locked condition, as it allows slip to penetrate. The plate coupling in the northern part of the margin, further north from East Cape, is not well constrained; here we assume VS conditions ($a - b > 0$ for 475 km $<$ Y $<$ 500 km in Figure 2a) in that region, which would lead to stable sliding. We also examine alternative parameterizations for the northern and southern ends of the model and discuss the results in Section 3.2.5.

The model parameter W, which measures the downdip width of the SSE zone, varies along the strike of the fault as shown in Figure 2c. Being an along-dip distance, this parameter is inversely proportional to the dip angle of the plate interface. Notably, W is widest in the southern part of the margin (Figure 2c), consistent with a shallower dip angle of the plate-boundary fault in that region (Barker et al., 2009).

3 Model Results

3.1 Parameter exploration

We first perform a total of 63 simulations, each of which takes at least 24 hours on 53 physical cores of the New Zealand eScience Infrastructure's Cray XC50 supercomputer, to explore a wide range of model parameters and identify a set of models that result in SSEs along the entire margin. As expected, depending on friction parameters a/b and the ratio W/h^*, the model leads to three different slip behaviors: (1) stable creep, (2) SSEs ($V > \sim 3$ Vpl$_{\text{ref}}$ or 0.39 mm/day), where Vpl$_{\text{ref}}$= 45 mm/year is a reference plate convergence velocity and (3) seismic events ($V > 5$ mm/s). The slip behavior is classified as 'seismic' when at least one seismic event arises in the first 20 SSE cycles, i.e. if the maximum velocity on the fault exceeds 5 mm/s before the first 20 SSEs have emerged. This condition is set to distinguish this slip pattern from simulations where SSEs are the primary mode of slip. We note that given that simulating earthquakes is computationally demanding with the numerical approach used in this study, we do not analyze SSE cycles after the emergence of seismic events.

Phase diagrams in Figures 3a to 3f show the slip behavior with respect to a/b and W_{ave}/h^*, where $W_{\text{ave}} = 87.5$ km is the average W along-strike, calculated from the profile in Figure 2c. We present the results for two different values of $\bar{\sigma}_n$ and $(a{-}b)_{\text{vw}}$ in the SSE zone (textbox on top of Figure 3). As the slip behavior often varies along the strike of the fault, to describe these variations we divide the fault into three major segments: northern, central and southern segments (red labels on the right in Figure 2). These segments loosely correspond to the along-strike ranges of SSEs' recurrence interval estimated from observations (dashed red lines in Figure 1b). For each simulation in Figure 3, we show the slip behavior at each of these segments in separate plots (e.g., Figure 3a to 3c), noting that they represent the same simulation case.

Phase diagrams for $\bar{\sigma}_n = 1$ MPa and $(a{-}b)_{\text{vw}} =$ -0.003 (Figure 3a to 3c) are qualitatively similar to those with $\bar{\sigma}_n = 10$ MPa and $(a{-}b)_{\text{vw}} =$ -0.0003 (Figure 3d to 3f). In both cases, the slip pattern changes along the strike of the fault. Notably, in the northern segment most simulation cases exhibit stable creep (black squares in Figure 3a and 3d), whereas in the southern segment SSEs are the predominant slip pattern (green triangles in Figure 3c and 3f). The difference in slip behavior at each fault segment is mainly controlled by the along-strike change in W, which is narrowest and widest in the northern and southern segments, respectively (Figure 2c). As h^* is assumed uniform along strike, a change in W leads to a change in W/h^*. Lower W/h^* results in stable creep, whereas larger W/h^* are required to generate SSEs, consistent with the numerical result of Liu and Rice (2007) and Barbot (2019).

SSE slip behavior emerges in all three segments only in a few simulations, which are indicated by the black dashed circles in Figure 3. Among these simulations, we select a model that best reproduces the observed characteristics of shallow SSEs (blue arrow in Figure 3). The parameters chosen for this model are given in Table 1. In the following, we describe the characteristics of SSEs in this preferred model and compare them with observations.

[Table 1 about here.]

[Figure 3 about here.]

3.2 Characteristics of SSEs in the preferred model and comparison with observations

3.2.1 Slip velocity evolution along the Hikurangi margin

The maximum slip rate on the fault, V_{max}, exhibits a complex evolution over time with peak velocities that span over three orders of magnitude (from $10^{-8.2}$ to $10^{-4.8}$ m/s) (Figure S2a). To visualize the slip behavior on the fault, we show snapshots of the slip velocity at successive time steps (Figure 4, Movie S1). As expected from the distribution of frictional properties on the fault (Figure 2a), the region with VS conditions slips steadily with velocities comparable to the plate rate (lightest brown color in Figure 4). The VW region, on the other hand, slips periodically through SSEs, which emerge spontaneously as patches of higher velocities (brown to dark brown colors in Figure 4). The region in-between SSEs is typically locked (dark blue colors in Figure 4). The degree of locking varies along the fault strike with the southern part of the margin being typically more strongly locked. The southern portion of the fault (0 km $<$ Y $<$ 50 km) slides at a rate only slightly below the plate rate at that region (lightest blue color in the southern part of the fault in Figure 4).

The distribution of modeled SSEs is consistent with geodetic observations, in that SSEs emerge as patches of high velocity nucleating at different locations along the margin. In Figure 4, SSEs (labeled with numbers) nucleate offshore Hawke's Bay (SSE 1 in Figure 4a), East Cape and Mahia Peninsula (SSE 2 and 3 in Figure 4b), Gisborne (SSE 4 in Figure 4e) and Cape Turnagain (SSE 5 in Figure 4g and 4h). These SSEs migrate along the fault as slip fronts (dashed arrows in Figure 4) and interact with each other. For instance, two slip fronts migrate towards each other in the northern part of the fault (converging dashed black arrows in Figure 4d) and coalesce in a velocity peak ($V_{max} >$ 10^{-7} m/s) that generates SSE 4 (Figure 4e). SSE 2 (Figure 4b) slowly migrates southwards (dashed black arrow in Figures 4b to 4f), which eventually leads to the nucleation of SSE 5 (Figure 4g). Geodetic observations have also identified along-strike migration of SSEs, for example, during the 2011 East Coast sequence, SSEs migrated episodically $\sim$300 km along-strike from offshore Castle Point to north of Gisborne (Wallace et al., 2012a).

To describe the long-term slow slip behavior along the margin, we show the slip velocity at 10 km depth over 100 years (Figure 5a and Figure S3). In this case, we assume a velocity threshold for SSEs of $\sim$3 Vpl_{ref} ($10^{-8.37}$ m/s or 0.39 mm/day). Although this threshold is below the lower resolution limit of onshore GPS networks ($\sim$2 mm/day), it allows us to describe several features of the modeled SSEs. In Figure 5a, SSEs emerge as bands that occur periodically along-strike (brown contours) and extend along most of the margin. Within each SSE, the slip rate can vary by a few orders of magnitude; high velocity patches (darker brown color in Figure 5b) are often linked up by regions of lower velocities (light brown color in Figure 5b). Some of these SSEs involve the interaction of multiple slip fronts that migrate along the fault (dark arrows in Figure 5b).

Modeled SSEs' recurrence interval varies along the fault strike. We calculate the recurrence interval of SSEs at three representative locations along the margin (P1, P2 and P3; Figure 5c). The average recurrence interval increases southward from 1.5 years at P1 (dashed blue line in Figure 5c) to almost 4 years at P3 (dashed black line in Figure 5c). This southward increase in the recurrence interval is broadly consistent with the observed pattern along the Hikurangi margin (Figure 1b). However, the recurrence intervals of modeled SSEs are slightly more variable in time during a given 20-year time interval than the observations (Figure 1b), especially in the southern part of the margin (P3 in Figure 5c).

Interestingly, peak slip rates at P1 to P3 increase southward along-strike (Figure S2b to S2d), which correlates with the change in SSEs' recurrence interval. The most frequent SSEs in the northern part of the margin have the lowest slip rates (Figure S2b), whereas the least frequent SSEs in the south have the highest slip rates (Figure S2d).

[Figure 4 about here.]

3.2.2 SSEs' source properties

To analyze the misfit between our model and observed SSEs, we calculate the source properties of simulated SSEs (i.e. duration, magnitude, maximum slip and maximum slip rate) and compare them with the observations. As source parameters depend on the resolution of SSEs' slip velocities of GPS observations at Hikurangi, we assume a velocity threshold of 20 $\mathrm{Vpl_{ref}}$ ($10^{-7.5}$ m/s or 2.46 mm/day), which is about the lower limit of resolved SSE velocities given in Ikari et al. (2020) catalog. SSE duration is defined as the time period over which the velocity threshold is exceeded. The corresponding SSE moment magnitude is calculated using the slip accumulated over the SSE duration and source area (defined as the region with slip greater than 2 cm). Note that we assume a shear modulus of 10 GPa to calculate the moment magnitude of simulated SSEs, consistent with the value used in Ikari et al. (2020) catalog, as well as estimates from Arnulf et al. (2021).

We find that the simulated SSE source properties agree well with the observations in all three segments (Figure 6). In particular, the model results in relatively low slip rates and moment magnitudes of SSEs in the northern part of the margin, consistent with observations (Todd & Schwartz, 2016; Ikari et al., 2020). This overall agreement of the simulated and observed SSE source properties is remarkable, given the relatively simple model considered here. The model shows a slightly broader range of duration, magnitudes and slip rates than those observed. This could be attributed to the longer time interval considered in the model (100 years) compared to geodetic observations, which cover only the last ∼20 years.

Seven synthetic SSEs ruptured more than one fault segment along-strike at irregular periods over the 100 years considered. Movie S2 shows an example of one multisegment SSE that ruptured both the southern and central segment. Compared to SSEs occuring in just one segment, multisegment SSEs have notably higher slip rate, magnitude and duration (multiple in Figure 6). We compare the source properties of multisegment SSEs with those of the 2016 East Coast SSE, triggered by the 2016 Kaikoura earthquake (Wallace et al., 2018), which ruptured ∼300 km along Hikurangi (Wallace et al., 2017, 2018). The magnitude and maximum slip of the observed triggered SSE are within the modeled ranges (yellow star in Figure 6), yet the durations are overpredicted. This suggests that spontaneous SSEs may last longer than dynamically triggered SSEs do. Comparing multisegment SSEs with observed spontaneous (i.e. not triggered) SSEs that rupture more than one segment along-strike (gray-shaded bar for multiple in Figure 6), we see that the model reproduces well their magnitudes and durations, but not their maximum slip and slip rates. We note that there are only 3 multisegment SSEs observed at

Hikurangi so far, and hence their source properties are not as well constrained as those of the individual SSEs.

[Figure 5 about here.]

[Figure 6 about here.]

3.2.3 Cumulative slip of SSEs and slip budget

To determine the slip distribution of modeled SSEs over time, we sum the slip of SSEs that exceeded the velocity threshold (20 Vpl_{ref}) within a given time period. Our results show that all the margin, between Cape Turnagain and Tolaga Bay slips during SSEs; however, the specific cumulative slip distribution varies at a decadal scale. Figures 7a to 7c show cumulative slip distribution over three 20-year time intervals. In Figure 7a, two large slip patches arise offshore Gisborne and Cape Turnagain with maximum cumulative slip of ∼70 cm and ∼50 cm, respectively. This pattern is qualitatively similar to the geodetic inversion of the cumulative slip distribution between 2002 and 2014 (Figure 1a), where two main slip patches develop at similar locations. At the same time, different cumulative SSE slip patterns emerge in other time intervals (Figures 7b and 7c). These results suggest that the slip distribution of shallow SSEs in Hikurangi may be variable over time.

To gain insight into the contribution of SSEs to the slip budget along the Hikurangi margin, we sum up the total cumulative slip released by SSEs over 100 years and divide it by the total amount of slip accumulated due to plate convergence over the same period. Our results (Figure 7d) show that the fault releases up to 60% of the plate convergence via SSEs, with most of the slip released at the central and southern sections of the fault, offshore Mahia Peninsula and Cape Turnagain. Notably, this percentage decreases to ∼20% in the northern section of the fault (Figure 5c), north of Gisborne, despite SSEs being more frequent in that region. This difference is attributable to the relatively lower slip rates of SSEs in the northern part of the margin (Figure S2b), as most of these events do not exceed the velocity threshold (20 $\mathrm{Vpl_{ref}}$), which causes the slip accumulated via SSEs to be comparatively low in that region. On the other hand, if we assume a velocity threshold of 3 $\mathrm{Vpl_{ref}}$, the percentage of slip released via SSEs is uniform within the SSE zone, from offshore East Cape to south of Cape Turnagain (Figure S4). In this case, SSEs release up to 90% of the slip accrued due to the plate convergence.

[Figure 7 about here.]

3.2.4 Best fit model with $\bar{\sigma}_n$ = 10 MPa in the SSE zone

We also compare the best fit model assuming $\bar{\sigma}_n$ = 10 MPa and $(a-b)$= -0.0003 in the SSE zone (orange arrow in Figure 3d to 3f) to observations. The parameters of this model are shown in Table 1. As in the preferred model with $\bar{\sigma}_n$ = 1 MPa and $(a-b)$= -0.003, this model reproduces the main features of shallow SSEs reasonably well (Figure 8). In particular, the along-strike segmentation of SSEs recurrence intervals are in good agreement with the observed pattern along Hikurangi (Figure 8b). On the other hand, modeled SSEs have slightly longer duration than observations (Figure 8c). The overall agreement between the models with a factor of 10 difference in $\bar{\sigma}_n$ suggests that the model results are not sensitive to $\bar{\sigma}_n$, but to the product $\bar{\sigma}_n(a-b)$.

[Figure 8 about here.]

3.2.5 Alternative model setups

To investigate the effect of some of our modeling assumptions on the results, we consider three alternative model setups, referred to as Alternative Model A, B and C. A detailed description of each setup is given in the supporting information (Text S2) and summarized in Table S1. For Alternative Model A, we consider an SSE zone that extends all the way to the trench, in contrast to the preferred model where the SSE zone starts at 4 km depth. This was motivated by the lack of constraints on the updip extent of shallow SSEs. For Alternative Model B, we assume a different parameter setting to better enforce the strongly locked condition in the southern part of the margin ($0 < Y < 50$ km), which in our preferred model slides only slightly below the plate rate. For Alternative Model C, we assume that the SSE zone extends along the entire length of the fault along-strike, thus we do not include the VW and VS bands on both sides of the model geometry, from 0 km < Y < 50 km and 475 km < Y < 500 km, respectively. This model allows to determine the effect of the parameter setting on the ends on the fault on SSEs' segmentation. The parameters chosen for each alternative model are the same as for the preferred model given in Table 1. We find that each alternative model reproduced the source properties of observed shallow SSEs (Figure S5 to S8). Some differences exist between the model results, for instance in Alternative model C, SSEs extent along the entire fault along-strike (i.e. 500 km). On the other hand, the along-strike change in the recurrence interval is broadly consistent with observations along Hikurangi for all three alternative models (Figure S5b, S7b and S8b). These findings demonstrate that the overall fitness of our model is not significantly affected by these assumptions.

3.3 Controls on along-strike segmentation of SSEs

To investigate the main factors that control the segmentation of SSE recurrence intervals, we consider additional three different model setups M2 – M4 (with M1 being the preferred model shown in Section 3.1). In M1, both the downdip width of the SSE zone (i.e. W) and the plate convergence rate vary along the strike of the fault (Section 2.2). To isolate the effect of a non-planar fault and spatially variable plate convergence, we construct model M2 that has a uniform plate convergence rate along the margin, which is set to $\mathrm{Vpl}_{\mathrm{ref}}$ (45 mm/yr), and Models M3 and M4 that have uniform W along-strike with either variable (M3) or uniform (M4) plate convergence rate. To set W uniform along the margin, we use the planar fault geometry (Figure 2d to 2f), described in the supplementary information (Text S3). For M3 and M4, we assume the same model parameters given in Table 1, except that $h^* = 115$ km and d_c =10.2 mm. In this case, W/h^*

= 0.77, which is comparable to the value in M1 and M2, where W/h^* ranges from 0.65 to 1.14 (for $h^* = 95$ km). Ensuring similar values of W/h^* for different simulation cases enables us to compare between model results without the influence of the differences in W/h^*. Table S2 summarizes the characteristics of each model setup.

To determine the effect of the different model setups on SSE segmentation, we compare the along-strike changes in the recurrence interval of SSEs between these four models (M1-M4). To do so, we calculate the recurrence interval of peak slip rates that exceed 3 $\mathrm{Vpl_{ref}}$ at the same three locations along the margin (P1, P2 and P3 for the non-planar fault and P1*, P2* and P3* for the planar fault, red circles in Figure 2a and 2d, respectively). We find that for M1 and M3, the northward increase in the plate convergence rate correlates with the decrease in the recurrence interval along the margin (Figure 9a and 9c). The segmentation of the recurrence interval is still present in M2 (Figure 9b), but vanishes in M4 (Figure 9d). This suggests that along-strike changes in W also contributes to the segmentation of the modeled SSEs. In particular, at P3, where W is the widest along the margin (Figure 2c), the recurrence intervals are the longest (Figure 9b), whereas the opposite is true for P1 (i.e. shortest recurrence interval and narrowest W), suggesting that W positively correlates with the recurrence interval.

[Figure 9 about here.]

4 Discussion

4.1 Along-strike segmentation of shallow SSEs in Hikurangi

Our results suggest that the along-strike change in the recurrence interval of shallow SSEs is controlled by spatial variations in both the downdip width of the SSE zone (i.e. model parameter W) and the plate convergence rate (V_{pl}) along the margin. The inverse correlation between the plate convergence rate and SSE recurrence interval (Figures 9a and 9c) is consistent with both previous numerical results (Shibazaki et al., 2012; Watkins et al., 2015; H. Li et al., 2018) and the following simple analysis. For quasi-periodic

SSEs recurring every T years, the recurrence interval T can be expressed as $T = \Delta\tau/\dot{\tau}$, where $\Delta\tau$ is the stress drop of quasi-periodic SSEs of the same magnitude and $\dot{\tau}$ is an inter-SSE stressing rate which would be proportional to V_{pl} (Kaneko et al., 2018). Since the stress drop of simulated SSEs are roughly constant, a faster convergence rate (larger V_{pl}) would result in a shorter recurrence interval. Hence the northward increase of the convergence rate along the Hikurangi margin (Wallace et al., 2004) likely contributes to the shorter recurrence interval of SSEs offshore Tolaga Bay in the north, compared to Cape Turnagain, ~350 km to the southeast.

In Section 3.3, we show that the recurrence interval of SSEs is also affected by spatially variable downdip width of the SSE zone (Figure 9). Assuming a uniform W along-strike leads to SSEs with less segmented recurrence intervals (Figure 9c and 9d), while for variable W along-strike, SSEs with longer recurrence intervals concentrate in the region with the widest W along the margin (Figure 9d). The positive correlation of W with SSEs' recurrence intervals is consistent with previous numerical results assuming both planar and non-planar faults (Liu & Rice, 2009; Shibazaki et al., 2012). The effect of W on shallow SSEs in Hikurangi could explain why their recurrence interval does not gradually increase along-strike, as would be expected if only the plate rate influenced them (e.g. Figure 9c). Instead, an abrupt increase in the recurrence interval takes place from the central (~1-2 years) to the southern (~5 years) part of the margin (Figure 1b), coinciding with the change in W along-strike (Figure 2c). Our results thus suggest that the effects of W and V_{pl} combine to enhance the segmentation of shallow SSEs. Although it is difficult to quantitatively assess which effect is dominant due to the nonlinearity of the model outcome, we note that the downdip width of the SSE zone appears to have a slightly stronger effect on the recurrence interval than the variable plate convergence rates, as variable W and uniform convergence rate leads to a stronger segmentation of the recurrence intervals than uniform W with variable plate convergence rates (compare Figures 9b and 9c).

Our results indicate that along-strike change in the dip angle of the plate interface also contributes to the segmentation of SSEs along Hikurangi, as the downdip width of the SSE zone is inversely related to the plate dip angle. This explains why SSEs with longer recurrence interval concentrate in the southern part of the margin, where the plate dip angle is shallower. Our results support a previous numerical model of SSEs in Cascadia (D. Li & Liu, 2016) indicating that the dip angle influences the along-strike segmentation of these events.

Our results do not rule out other potential factors that could affect shallow SSE segmentation along the Hikurangi margin. For instance, along-strike changes in the effective normal stress have been linked to changes in the recurrence interval of simulated SSEs (Liu, 2014; H. Li et al., 2018). Along the Hikurangi margin, these changes are not well constrained, and further research is required to determine whether this factor could contribute to SSE segmentation as well. In Section 4.4, we elaborate on other factors that were not considered in our modeling.

4.2 Implications for megathrust slip behavior and SSE environment in Hikurangi

We estimate that modeled SSEs offshore the east coast of the North Island release up to 60% of the plate convergence rate over 100 years (Figure 7d), which suggests that SSEs are the main mechanism of strain release along the Hikurangi margin, consistent with geodetic inferences (Wallace & Beavan, 2010). We find that the estimation of the slip budget depends on the velocity threshold assumed to define SSEs; assuming a slip-rate threshold about six times lower, the modeled SSEs release up to 90% of the slip deficit (Figure S4). This result suggests that the resolution limit of GPS inversion models strongly influences the assessment of the contribution of SSEs to the total slip deficit. This is especially relevant in Hikurangi, where most of the slip during shallow SSEs concentrates offshore, away from the inland geodetic network.

Our model suggests that shallow SSEs interact with each other along the Hikurangi margin. We see that both the initiation and arrest of an SSE usually involves the migration of slip fronts from or towards different regions along the fault (e.g. Movie S1 and Figure 5b). Some SSEs occur simultaneously (SSE 2 and 3 in Figure 4) or spatially close to each other (SSE 1 and 2 in Figure 4). In other instances, two slip fronts merge into a single large SSE (Figure 4d and 4e), a behavior that is comparable to the coalescence of slow slip fronts observed in Cascadia (Bletery & Nocquet, 2020) and that has been linked to the initiation of earthquakes (Kaneko & Ampuero, 2011; Bletery & Nocquet, 2020). All this indicates that our simulated SSEs are typically not separated in time and space, thus they are likely to have strong stress interactions between each other (Liu, 2014). These stress interactions may influence the seismicity and tectonic tremor rates that accompany some shallow SSE sequences in Hikurangi (e.g. Kim et al., 2011; Wallace et al., 2012a; Bartlow et al., 2014; Jacobs et al., 2016; Todd & Schwartz, 2016; Romanet & Ide, 2019).

Our model suggests that some shallow SSEs may rupture the whole margin along-strike, as shown in Figure 5a. These events would involve several subevents with faster slip (darker brown color in Figure 5b), which are linked up spatially by slower-slipping regions. Although these whole-margin SSEs have not been documented at Hikurangi, except for the SSE sequence triggered by the 2016 Kaikoura earthquake (Wallace et al., 2016), this lack of observations could be attributed to the limited resolution of the onshore geodetic network. These networks could only resolve the higher-velocity patches, as seen in Figure 4 (SSEs 1-5), while the slower-slipping regions in between these patches —where the slip rate is slightly larger than $\sim$3 $\mathrm{Vpl_{ref}}$ (0.39 mm/day) —would be below the detection threshold ($\sim$2 mm/day). For example, the observed shallow SSE sequence in 2011, where several SSEs of short duration (1-3 weeks) migrated northward along the margin over six months (Wallace et al., 2012a), could be a consequence of a whole-margin SSE of which only the high-velocity patches were detected.

Previous modelling studies have assumed near-lithostatic values of fluid pressure ($\bar{\sigma}_n$ ~1 MPa) in the source region of shallow SSEs in Hikurangi (Wei et al., 2018; Shibazaki et al., 2019). In contrast, our results suggest that the effective normal stress ($\bar{\sigma}_n$) could range from 1 to 10 MPa. The overall agreement between the models with a factor of 10 difference in $\bar{\sigma}_n$ (Figures 3, 6 and 8) suggests that pore fluid pressure in the SSE source region does not need to be a near-lithostatic value as long as the product $\bar{\sigma}_n(a-b)_{\mathrm{vw}}$ remains the same. A sub-lithostatic pore fluid pressure is also supported by a recently inferred range of $\bar{\sigma}_n$ (10-30 MPa) on the shallow portion of Hikurangi margin (Arnulf et al., 2021).

4.3 SSE source scaling relations

Scaling relations are often used to gain insight into the failure mechanism of SSEs, and how it differs from that of fast earthquakes. Based on a global compilation of slow earthquakes, the moment-duration scaling of SSEs was originally proposed to follow a linear scaling (M $\sim$ T) (Ide et al., 2007), which contrasts to the cubic scaling (M $\sim$ T^3) followed by earthquakes over a wide range of magnitudes (Kanamori & Anderson, 1975). Yet recent observations report a cubic moment-duration scaling of SSEs in Cascadia (Michel et al., 2019), Nankai (Takagi et al., 2019) and Mexico (Frank & Brodsky, 2019) subduction zones, as well as in the San Andreas fault (Tan & Marsan, 2020). Although the same cubic moment-duration scaling between earthquakes and SSEs could be due to different underlying reasons (Dal Zilio et al., 2020).

To determine the scaling relations of shallow SSEs, we take the Hikurangi SSE catalogue of Ikari et al. (2020) and plot the moment (M) versus duration (T), and also versus area (A) (Figure 10). We then compare these observed source properties with those of the simulated SSEs in our preferred model described in Section 3. We find that the source properties of observed shallow SSEs (yellow stars in Figure 10) broadly overlap with those simulated SSEs (triangles in Figure 10), further validating our model. As expected, the source properties of deep SSEs (green triangles in Figure 10) show larger moment magnitudes and duration than the shallow SSEs. The observed source properties of shallow SSEs in Hikurangi do not show a clear trend, which could be due to a limited range of durations and moments sampled by the shallow SSEs, as well as a short catalog (<20 years). Unlike their shallow counterparts, deep SSEs follow a distinguishable linear trend of the moment with respect to duration, with a best-fit scaling of M $= T^{1.95} \times 10^{19.5}$ (magenta line in Figure 10). A larger catalog is needed to determine whether shallow SSEs would also follow this trend.

The scaling trends of simulated shallow SSEs are clearer than for the observed shallow events. The best-fit moment-area relation of simulated SSEs follows $M \sim A^{1.39}$ (Figure 10b), which is close to the best fit exponent of 1.5 found in previous models of SSEs (Liu, 2014; Dal Zilio et al., 2020). On the other hand, the moment of simulated SSEs scales with the duration with an exponent of 1.65 (Figure 10a), although the scattering of the triangles makes it hard to define a linear trend. This scaling relation is comparable to $M \sim T^{1.3}$ found by previous SSE models (Shibazaki et al., 2012; Liu, 2014); our relatively larger exponent could be attributed to the interaction between slip fronts along the margin, which as shown by Liu (2014) leads to a scaling exponent closer to 2. To test the sensitivity of our results to the velocity threshold, we calculated the scaling relations assuming two additional thresholds (i.e., 15 Vpl_{ref} and 25 Vpl_{ref}) and find only slight differences in the scaling exponents ($< \pm 0.15$) (Figure S9). We hypothesize that the fact that the moment-duration scaling of our simulated SSEs ($M \sim T^{1.65}$) falls in between the previously-reported cubic and linear scalings could indicate that the scaling properties of SSEs are probably less clear-cut than commonly expected. If true, it would suggest that factors such as the source depth of SSEs or their tectonic environment could also affect their scaling relations.

[Figure 10 about here.]

4.4 Model limitations

Our modeling approach involves several assumptions and simplifications. As a first approximation, we assume that the frictional properties at the source depths of shallow SSEs are spatially homogeneous. However, rock-friction experiments using material entering the SSE source region at the Hikurangi margin indicate that the spatial distribution of frictional properties is likely more complex, as input sediments exhibit contrasting lithological (Barnes et al., 2020) and frictional properties (Boulton et al., 2019; Rabinowitz et al., 2018). Future modeling studies may account for frictional heterogeneity by modeling patches of velocity-weakening and velocity-strengthening materials, or by implementing a relative strength ratio that accounts for the proportions of these materials (Luo & Ampuero, 2018; Boulton et al., 2019; Barnes et al., 2020).

Our model geometry represents a smooth plate interface and ignores the geometric complexity in the region where shallow SSEs occur along the Hikurangi margin. Such complexity has been imaged by active source seismic studies offshore Gisborne, where significant relief (> 2 km) and roughness of the basement surface (Barnes et al., 2020), and the presence of seamounts (Bell et al., 2010) have been inferred. These findings together with the fact that several shallow SSEs in other subduction zones are also associated with rough plate interfaces (Wang & Bilek, 2014; Saffer & Wallace, 2015) suggests that accounting for smaller-scale roughness may play an important role in the generation mechanism of shallow SSEs (Sun et al., 2020; Romanet et al., 2018).

Following the classic rate-and-state friction formulation (Text S1), our model assumes that friction parameter $(a{-}b)$ and the critical slip distance (d_c) are independent of the sliding velocity. In contrast, laboratory measurements on drill samples from different subduction zones, including Hikurangi, show a systematic variation of $(a{-}b)$ and d_c with slip velocity (Ikari et al., 2009; Ikari & Saffer, 2011; Rabinowitz et al., 2018; Boulton et al., 2019). A recent numerical model accounting for this slip-rate dependence of $(a{-}b)$ and d_c successfully reproduced SSEs characteristics over a broader range of parameters than with the classic rate-and-state formulation (Im et al., 2020). This could explain why the parameter range that can reproduce SSEs comparable to observations is relatively narrow in our model (Section 3.1).

Our modeling approach assumes that the effective normal stress is independent of time at the source depths of shallow SSEs, an assumption commonly invoked by numerical models of SSEs (e.g. Liu & Rice, 2009; Shibazaki et al., 2012; Matsuzawa et al., 2013; Shibazaki et al., 2019). Yet recent observations in Nankai (Nakajima & Uchida, 2018), Cascadia (Gosselin et al., 2020), Mexico (Frank et al., 2015) and Hikurangi (Warren-Smith et al., 2019; Zal et al., 2020) subduction zones inferred temporal changes of pore fluid pressure and hence the effective normal stress during and inter-SSE periods. These changes are attributed to a fault valving behavior (Sibson, 1990, 1992) that possibly results from cyclical permeability changes induced by slip during SSEs (Nakajima & Uchida, 2018; Warren-Smith et al., 2019; Gosselin et al., 2020; Zal et al., 2020). Future modeling work accounting for fluid valving behavior in simulations of Hikurangi SSEs is needed.

5 Conclusions

We have investigated the cause of along-strike changes in the source properties of shallow slow slip events (SSEs) along the Hikurangi margin using numerical simulations of fault slip that incorporate rate-and-state friction laws and non-planar fault geometry. Our model reproduces the magnitude and duration of shallow SSEs, as well as the segmentation of their recurrence intervals, which increases southward along the strike of the margin.

Our model results indicate that along-strike variations in both the plate convergence rate and the downdip width of the region of low effective normal stress (or SSE zone), play an important role in the segmentation of SSE recurrence intervals along the Hikurangi margin. We find that a wider SSE zone and a lower plate convergence rate favor SSE cycles with long recurrence interval. This could explain why shallow SSEs offshore Cape Turnagain, where the plate convergence rate and the SSE zone are respectively lower and wider than further north along strike, have longer recurrence interval ($\sim$ 5 years) than elsewhere along the margin (1-2 years). Moreover, the shallow dipping angle of the plate interface in this portion of the margin contributes to a wider downdip width of the SSE zone, which indicates that along-strike variations in the plate geometry also promote the segmentation of these events.

Our results show that the cumulative slip distribution of modeled SSEs is variable over a decadal scale, as SSE slip patches concentrate at different locations along the margin at different time intervals. This result suggests that slip distribution of shallow SSEs along Hikurangi may also vary in the future.

We have found that effective normal stresses ($\bar{\sigma}_n$) of 1 MPa and 10 MPa lead to similar slip behaviors if we adjust the friction parameter $(a-b)_{\text{vw}}$ such that the product $\bar{\sigma}_n(a-b)_{\text{vw}}$ remains constant. In addition, models assuming either $\bar{\sigma}_n = 1$ or 10 MPa in the SSE zone reproduce the main features of shallow SSEs in Hikurangi. These results imply that $\bar{\sigma}_n$ need not be as low as 1 MPa at the source depths of shallow SSEs, contrary to the assumptions of several previous modelling studies.

Acknowledgments

This work was supported by the Rutherford Discovery Fellowship from the Royal Society of New Zealand and the Ministry of Business, Innovation and Employment (MBIE) grant (gns/mbie00053). Computing resources were provided by the New Zealand eScience Infrastructure (NeSI) high-performance computing facilities. D.L. is supported by the European Research Council (ERC) Starting Grant TEAR agreement (No. 852992) under the European Union's Horizon 2020 research and innovation programme. The authors thank Dr. Carolyn Boulton and Katie Woods for their helpful comments on the work. The data used to produce the figures is available at `https://doi.org/10.5281/zenodo.5143825`.

References

Araki, E., Saffer, D. M., Kopf, A. J., Wallace, L. M., Kimura, T., Machida, Y., ... others (2017). Recurring and triggered slow-slip events near the trench at the Nankai Trough subduction megathrust. *Science*, *356*(6343), 1157–1160. doi: 10.1126/science.aan3120.

Arnulf, A. F., Biemiller, J., Lavier, L., Wallace, L. M., Bassett, D., Henrys, S., ... Faverola, A. P. (2021). Physical conditions and frictional properties in the source region of a slow-slip event. *Nature Geoscience*, *14*, 334–340. doi: 10.1038/s41561-021-00741-0.

Audet, P., Bostock, M. G., Christensen, N. I., & Peacock, S. M. (2009). Seismic evidence for overpressured subducted oceanic crust and megathrust fault sealing. *Nature*, *457*(7225), 76–78. doi: 10.1038/nature07650.

Audet, P., & Bürgmann, R. (2014). Possible control of subduction zone slow-earthquake periodicity by silica enrichment. *Nature*, *510*(7505), 389–392. doi: 10.1038/nature13391.

Audet, P., & Kim, Y. (2016). Teleseismic constraints on the geological environment of deep episodic slow earthquakes in subduction zone forearcs: A review. *Tectonophysics*, *670*, 1–15. doi: 10.1016/j.tecto.2016.01.005.

Barbot, S. (2019). Slow-slip, slow earthquakes, period-two cycles, full and partial ruptures, and deterministic chaos in a single asperity fault. *Tectonophysics*, *768*, 228171. doi: 10.1016/j.tecto.2019.228171.

Barker, D. H., Sutherland, R., Henrys, S., & Bannister, S. (2009). Geometry of the Hikurangi subduction thrust and upper plate, North Island, New Zealand. *Geochemistry, Geophysics, Geosystems*, *10*, Q02007. doi: 10.1029/2008GC002153.

Barnes, P. M., Wallace, L. M., Saffer, D. M., Bell, R. E., Underwood, M. B., Fagereng, A., ... others (2020). Slow slip source characterized by lithological and geometric heterogeneity. *Science Advances*, *6*(13), eaay3314. doi:

10.1126/sciadv.aay3314.

Bartlow, N. M. (2020). A long-term view of episodic tremor and slip in Cascadia. *Geophysical Research Letters*, *47*(3), e2019GL085303. doi: 10.1029/2019GL085303.

Bartlow, N. M., Wallace, L. M., Beavan, R. J., Bannister, S., & Segall, P. (2014). Time-dependent modeling of slow slip events and associated seismicity and tremor at the Hikurangi subduction zone, New Zealand. *Journal of Geophysical Research: Solid Earth*, *119*(1), 734–753. doi: 10.1002/2013JB010609.

Bassett, D., Sutherland, R., & Henrys, S. (2014). Slow wavespeeds and fluid overpressure in a region of shallow geodetic locking and slow slip, Hikurangi subduction margin, New Zealand. *Earth and Planetary Science Letters*, *389*, 1–13. doi: 10.1016/j.epsl.2013.12.021.

Bell, R., Sutherland, R., Barker, D. H., Henrys, S., Bannister, S., Wallace, L., & Beavan, J. (2010). Seismic reflection character of the Hikurangi subduction interface, New Zealand, in the region of repeated Gisborne slow slip events. *Geophysical Journal International*, *180*(1), 34–48. doi: 10.1111/j.1365-246X.2009.04401.x.

Beroza, G. C., & Ide, S. (2011). Slow earthquakes and nonvolcanic tremor. *Annual Review of Earth and Planetary Sciences*, *39*, 271–296. doi: 10.1146/annurev-earth-040809-152531.

Blanpied, M., Marone, C., Lockner, D., Byerlee, J., & King, D. (1998). Quantitative measure of the variation in fault rheology due to fluid-rock interactions. *Journal of Geophysical Research: Solid Earth*, *103*(B5), 9691–9712. doi: 10.1029/98JB00162.

Bletery, Q., & Nocquet, J.-M. (2020). Slip bursts during coalescence of slow slip events in Cascadia. *Nature Communications*, *11*, 2159. doi: 10.1038/s41467-020-15494-4.

Boulton, C., Niemeijer, A. R., Hollis, C. J., Townend, J., Raven, M. D., Kulhanek,

D. K., & Shepherd, C. L. (2019). Temperature-dependent frictional properties of heterogeneous Hikurangi Subduction Zone input sediments, ODP Site 1124. *Tectonophysics*, *757*, 123–139. doi: 10.1016/j.tecto.2019.02.006.

Brooks, B. A., Foster, J. H., Bevis, M., Frazer, L. N., Wolfe, C. J., & Behn, M. (2006). Periodic slow earthquakes on the flank of Kīlauea volcano, Hawaii. *Earth and Planetary Science Letters*, *246*(3-4), 207–216. doi: 10.1016/j.epsl.2006.03.035.

Brudzinski, M. R., & Allen, R. M. (2007). Segmentation in episodic tremor and slip all along Cascadia. *Geology*, *35*(10), 907–910. doi: 10.1130/G23740A.1.

Cervelli, P., Segall, P., Johnson, K., Lisowski, M., & Miklius, A. (2002). Sudden aseismic fault slip on the south flank of Kilauea volcano. *Nature*, *415*(6875), 1014–1018. doi: doi.org/10.1038/4151014a.

Dal Zilio, L., Lapusta, N., & Avouac, J.-P. (2020). Unraveling scaling properties of slow-slip events. *Geophysical Research Letters*, *47*(10), e2020GL087477. doi: 10.1029/2020GL087477.

Dieterich, J. H. (1979). Modeling of rock friction: 1. Experimental results and constitutive equations. *Journal of Geophysical Research: Solid Earth*, *84*(B5), 2161–2168. doi: 10.1029/JB084iB05p02161.

Dixon, T. H., Jiang, Y., Malservisi, R., McCaffrey, R., Voss, N., Protti, M., & Gonzalez, V. (2014). Earthquake and tsunami forecasts: Relation of slow slip events to subsequent earthquake rupture. *Proceedings of the National Academy of Sciences USA*, *111*(48), 17039–17044. doi: 10.1073/pnas.1412299111.

Douglas, A., Beavan, J., Wallace, L., & Townend, J. (2005). Slow slip on the northern Hikurangi subduction interface, New Zealand. *Geophysical Research Letters*, *32*(16). doi: 10.1029/2005GL023607.

Dragert, H., Wang, K., & Rogers, G. (2004). Geodetic and seismic signatures of episodic tremor and slip in the northern Cascadia subduction zone. *Earth Planets Space*, *56*(12), 1143–1150. doi: 10.1186/BF03353333.

Eberhart-Phillips, D., & Bannister, S. (2015). 3-D imaging of the northern Hikurangi subduction zone, New Zealand: variations in subducted sediment, slab fluids and slow slip. *Geophysical Journal International*, *201*(2), 838–855. doi: 10.1093/gji/ggv057.

Eberhart-Phillips, D., Bannister, S., & Reyners, M. (2017). Deciphering the 3-D distribution of fluid along the shallow Hikurangi subduction zone using P-and S-wave attenuation. *Geophysical Journal International*, *211*(2), 1032–1045. doi: 10.1093/gji/ggx348.

Frank, W. B., & Brodsky, E. E. (2019). Daily measurement of slow slip from low-frequency earthquakes is consistent with ordinary earthquake scaling. *Science advances*, *5*(10), eaaw9386. doi: 10.1126/sciadv.aaw9386.

Frank, W. B., Shapiro, N. M., Husker, A. L., Kostoglodov, V., Bhat, H. S., & Campillo, M. (2015). Along-fault pore-pressure evolution during a slow-slip event in Guerrero, Mexico. *Earth and Planetary Science Letters*, *413*, 135–143. doi: 10.1016/j.epsl.2014.12.051.

Fu, Y., & Freymueller, J. T. (2013). Repeated large slow slip events at the southcentral Alaska subduction zone. *Earth and Planetary Science Letters*, *375*, 303–311. doi: 10.1016/j.epsl.2013.05.049.

Fu, Y., Liu, Z., & Freymueller, J. T. (2015). Spatiotemporal variations of the slow slip event between 2008 and 2013 in the southcentral Alaska subduction zone. *Geochemistry, Geophysics, Geosystems*, *16*(7), 2450–2461. doi: 10.1002/2015GC005904.

Gosselin, J. M., Audet, P., Estève, C., McLellan, M., Mosher, S. G., & Schaeffer, A. J. (2020). Seismic evidence for megathrust fault-valve behavior during episodic tremor and slip. *Science Advances*, *6*(4), eaay5174. doi: 10.1126/sciadv.aay5174.

Graham, S., DeMets, C., Cabral-Cano, E., Kostoglodov, V., Rousset, B., Walpersdorf, A., … Salazar-Tlaczani, L. (2016). Slow Slip History for the MEXICO

Subduction Zone: 2005 Through 2011. *Pure and Applied Geophysics*, *173*, 3445–3465. doi: 10.1007/s00024-015-1211-x.

Heise, W., Caldwell, T., Bannister, S., Bertrand, E., Ogawa, Y., Bennie, S., & Ichihara, H. (2017). Mapping subduction interface coupling using magnetotellurics: Hikurangi margin, New Zealand. *Geophysical Research Letters*, *44*(18), 9261–9266. doi: 10.1002/2017GL074641.

Heise, W., Caldwell, T. G., Bertrand, E. A., Hill, G. J., Bennie, S. L., & Ogawa, Y. (2013). Changes in electrical resistivity track changes in tectonic plate coupling. *Geophysical Research Letters*, *40*(19), 5029–5033. doi: 10.1002/grl.50959.

Hirose, H., & Obara, K. (2005). Repeating short-and long-term slow slip events with deep tremor activity around the Bungo channel region, southwest Japan. *Earth, Planets and Space*, *57*(10), 961–972. doi: 10.1186/BF03351875.

Ide, S., Beroza, G. C., Shelly, D. R., & Uchide, T. (2007). A scaling law for slow earthquakes. *Nature*, *447*(7140), 76–79. doi: 10.1038/nature05780.

Ikari, M. J., & Saffer, D. M. (2011). Comparison of frictional strength and velocity dependence between fault zones in the Nankai accretionary complex. *Geochemistry, Geophysics, Geosystems*, *12*(4), Q0AD11. doi: 10.1029/2010GC003442.

Ikari, M. J., Saffer, D. M., & Marone, C. (2009). Frictional and hydrologic properties of clay-rich fault gouge. *Journal of Geophysical Research: Solid Earth*, *114*, B05409. doi: 10.1029/2008JB006089.

Ikari, M. J., Wallace, L. M., Rabinowitz, H. S., Savage, H. M., Hamling, I. J., & Kopf, A. J. (2020). Observations of laboratory and natural slow slip events: Hikurangi subduction zone, New Zealand. *Geochemistry, Geophysics, Geosystems*, *21*(2), e2019GC008717. doi: 10.1029/2019GC008717.

Im, K., Saffer, D., Marone, C., & Avouac, J.-P. (2020). Slip-rate-dependent friction as a universal mechanism for slow slip events. *Nature Geoscience*, *13*(10), 705–710. doi: 10.1038/s41561-020-0627-9.

Jacobs, K., Savage, M., & Smith, E. (2016). Quantifying seismicity associated with slow slip events in the Hikurangi margin, New Zealand. *New Zealand Journal of Geology and Geophysics*, *59*(1), 58–69. doi: 10.1080/00288306.2015.1127827 .

Kanamori, H., & Anderson, D. L. (1975). Theoretical basis of some empirical relations in seismology. *Bulletin of the seismological society of America*, *65*(5), 1073–1095.

Kaneko, Y., & Ampuero, J.-P. (2011). A mechanism for preseismic steady rupture fronts observed in laboratory experiments. *Geophysical Research Letters*, *38*, L21307. doi: 10.1029/2011GL049953.

Kaneko, Y., Wallace, L. M., Hamling, I. J., & Gerstenberger, M. C. (2018). Simple physical model for the probability of a subduction-zone earthquake following slow slip events and earthquakes: Application to the Hikurangi megathrust, New Zealand. *Geophysical Research Letters*, *45*(9), 3932–3941. doi: 10.1029/2018GL077641.

Kato, A., Obara, K., Igarashi, T., Tsuruoka, H., Nakagawa, S., & Hirata, N. (2012). Propagation of slow slip leading up to the 2011 M_w 9.0 Tohoku-Oki earthquake. *Science*, *335*(6069), 705–708. doi: 10.1126/science.1215141.

Kim, M. J., Schwartz, S. Y., & Bannister, S. (2011). Non-volcanic tremor associated with the March 2010 Gisborne slow slip event at the Hikurangi subduction margin, New Zealand. *Geophysical Research Letters*, *38*(14). doi: 10.1029/2011GL048400.

Kodaira, S., Iidaka, T., Kato, A., Park, J.-O., Iwasaki, T., & Kaneda, Y. (2004). High pore fluid pressure may cause silent slip in the Nankai Trough. *Science*, *304*(5675), 1295–1298. doi: 10.1126/science.1096535.

Lapusta, N., Rice, J. R., Ben-Zion, Y., & Zheng, G. (2000). Elastodynamic analysis for slow tectonic loading with spontaneous rupture episodes on faults with rate-and state-dependent friction. *Journal of Geophysical Research: Solid*

Earth, *105*(B10), 23765–23789. doi: 10.1029/2000JB900250.

Li, D., & Liu, Y. (2016). Spatiotemporal evolution of slow slip events in a nonplanar fault model for northern Cascadia subduction zone. *Journal of Geophysical Research: Solid Earth*, *121*(9), 6828–6845. doi: 10.1002/2016JB012857.

Li, D., & Liu, Y. (2017). Modeling slow-slip segmentation in Cascadia subduction zone constrained by tremor locations and gravity anomalies. *Journal of Geophysical Research: Solid Earth*, *122*(4), 3138–3157. doi: 10.1002/2016JB013778 .

Li, H., Wei, M., Li, D., Liu, Y., Kim, Y., & Zhou, S. (2018). Segmentation of slow slip events in south central Alaska possibly controlled by a subducted oceanic plateau. *Journal of Geophysical Research: Solid Earth*, *123*(1), 418–436. doi: 10.1002/2017JB014911.

Linde, A. T., Gladwin, M. T., Johnston, M. J., Gwyther, R. L., & Bilham, R. G. (1996). A slow earthquake sequence on the San Andreas fault. *Nature*, *383*(6595), 65–68. doi: 10.1038/383065a0.

Liu, Y. (2014). Source scaling relations and along-strike segmentation of slow slip events in a 3-D subduction fault model. *Journal of Geophysical Research: Solid Earth*, *119*(8), 6512–6533. doi: 10.1002/2014JB011144.

Liu, Y., & Rice, J. R. (2007). Spontaneous and triggered aseismic deformation transients in a subduction fault model. *Journal of Geophysical Research: Solid Earth*, *112*, B09404. doi: 10.1029/2007JB004930.f.

Liu, Y., & Rice, J. R. (2009). Slow slip predictions based on granite and gabbro friction data compared to GPS measurements in northern Cascadia. *Journal of Geophysical Research: Solid Earth*, *114*, B09407. doi: 10.1029/2008JB006142.

Lowry, A. R., Larson, K. M., Kostoglodov, V., & Bilham, R. (2001). Transient fault slip in Guerrero, southern Mexico. *Geophysical Research Letters*, *28*(19), 3753–3756. doi: 10.1029/2001GL013238.

Luo, Y., & Ampuero, J.-P. (2018). Stability of faults with heterogeneous friction properties and effective normal stress. *Tectonophysics*, *733*, 257–272. doi: 10.1016/j.tecto.2017.11.006.

Matsuzawa, T., Hirose, H., Shibazaki, B., & Obara, K. (2010). Modeling short-and long-term slow slip events in the seismic cycles of large subduction earthquakes. *Journal of Geophysical Research: Solid Earth*, *115*, B12301. doi: 10.1029/2010JB007566.

Matsuzawa, T., Shibazaki, B., Obara, K., & Hirose, H. (2013). Comprehensive model of short-and long-term slow slip events in the Shikoku region of Japan, incorporating a realistic plate configuration. *Geophysical Research Letters*, *40*(19), 5125–5130. doi: 10.1002/grl.51006.

Michel, S., Gualandi, A., & Avouac, J.-P. (2019). Similar scaling laws for earthquakes and Cascadia slow-slip events. *Nature*, *574*(7779), 522–526. doi: 10.1038/s41586-019-1673-6.

Nakajima, J., & Uchida, N. (2018). Repeated drainage from megathrusts during episodic slow slip. *Nature Geoscience*, *11*(5), 351–356. doi: 10.1038/s41561-018-0090-z.

Obara, K. (2010). Phenomenology of deep slow earthquake family in southwest Japan: Spatiotemporal characteristics and segmentation. *Journal of Geophysical Research: Solid Earth*, *115*(B00A25). doi: 10.1029/2008JB006048.

Obara, K., Hirose, H., Yamamizu, F., & Kasahara, K. (2004). Episodic slow slip events accompanied by non-volcanic tremors in southwest Japan subduction zone. *Geophysical Research Letters*, *31*, L23602. doi: 10.1029/2004GL020848.

Ohta, Y., Freymueller, J. T., Hreinsdóttir, S., & Suito, H. (2006). A large slow slip event and the depth of the seismogenic zone in the south central Alaska subduction zone. *Earth and Planetary Science Letters*, *247*(1-2), 108–116. doi: 10.1016/j.epsl.2006.05.013.

Outerbridge, K. C., Dixon, T. H., Schwartz, S. Y., Walter, J. I., Protti, M., Gonzalez, V., ... Rabbel, W. (2010). A tremor and slip event on the Cocos-

Caribbean subduction zone as measured by a global positioning system (GPS) and seismic network on the Nicoya Peninsula, Costa Rica. *Journal of Geophysical Research: Solid Earth*, *115*, B10408. doi: 10.1029/2009JB006845.

Perez-Silva, A., Li, D., Gabriel, A.-A., & Kaneko, Y. (2021). 3D Modeling of long-term slow slip events along the flat-slab segment in the Guerrero Seismic Gap, Mexico. *Geophysical Research Letters*, *48*(13), e2021GL092968. doi: 10.1029/2021GL092968.

Rabinowitz, H., Savage, H., Skarbek, R., Ikari, M. J., Carpenter, B. M., & Collettini, C. (2018). Frictional behavior of input sediments to the Hikurangi Trench, New Zealand. *Geochemistry, Geophysics, Geosystems*, *19*(9), 2973–2990. doi: 10.1029/2018GC007633.

Radiguet, M., Cotton, F., Vergnolle, M., Campillo, M., Walpersdorf, A., Cotte, N., & Kostoglodov, V. (2012). Slow slip events and strain accumulation in the Guerrero gap, Mexico. *Journal of Geophysical Research: Solid Earth*, *117*, B04305. doi: 10.1029/2011JB008801.

Radiguet, M., Perfettini, H., Cotte, N., Gualandi, A., Valette, B., Kostoglodov, V., … Campillo, M. (2016). Triggering of the 2014 M_w 7.3 Papanoa earthquake by a slow slip event in Guerrero, Mexico. *Nature Geoscience*, *9*(11), 829–833. doi: 10.1038/ngeo2817.

Rice, J. R. (1993). Spatio-temporal complexity of slip on a fault. *Journal of Geophysical Research: Solid Earth*, *98*(B6), 9885–9907. doi: 10.1029/93JB00191.

Romanet, P., Bhat, H. S., Jolivet, R., & Madariaga, R. (2018). Fast and slow slip events emerge due to fault geometrical complexity. *Geophysical Research Letters*, *45*(10), 4809–4819. doi: 10.1029/2018GL077579.

Romanet, P., & Ide, S. (2019). Ambient tectonic tremors in Manawatu, Cape Turnagain, Marlborough, and Puysegur, New Zealand. *Earth, Planets and Space*, *71*, 59. doi: 10.1186/s40623-019-1039-1.

Rousset, B., Bürgmann, R., & Campillo, M. (2019). Slow slip events in the roots of the San Andreas fault. *Science advances*, *5*(2), eaav3274. doi: 10.1126/sciadv.aav3274.

Rubin, A. M. (2008). Episodic slow slip events and rate-and-state friction. *Journal of Geophysical Research: Solid Earth*, *113*, B11414. doi: 10.1029/2008JB005642

Rubin, A. M., & Ampuero, J.-P. (2005). Earthquake nucleation on (aging) rate and state faults. *Journal of Geophysical Research: Solid Earth*, *110*, B11312. doi: 10.1029/2005JB003686.

Ruiz, S., Metois, M., Fuenzalida, A., Ruiz, J., Leyton, F., Grandin, R., ... Campos, J. (2014). Intense foreshocks and a slow slip event preceded the 2014 Iquique M_w 8.1 earthquake. *Science*, *345*(6201), 1165–1169. doi: 10.1126/science.1256074.

Saffer, D. M., & Wallace, L. M. (2015). The frictional, hydrologic, metamorphic and thermal habitat of shallow slow earthquakes. *Nature Geoscience*, *8*(8), 594–600. doi: 10.1038/ngeo2490.

Scholz, C. H. (1998). Earthquakes and friction laws. *Nature*, *391*(6662), 37–42. doi: 10.1038/34097.

Schwartz, S. Y., & Rokosky, J. M. (2007). Slow slip events and seismic tremor at circum-Pacific subduction zones. *Reviews of Geophysics*, *45*, RG3004. doi: 10.1029/2006RG000208.

Segall, P., Desmarais, E. K., Shelly, D., Miklius, A., & Cervelli, P. (2006). Earthquakes triggered by silent slip events on Kīlauea volcano, Hawaii. *Nature*, *442*(7098), 71–74. doi: 10.1038/nature04938.

Shibazaki, B., Obara, K., Matsuzawa, T., & Hirose, H. (2012). Modeling of slow slip events along the deep subduction zone in the Kii Peninsula and Tokai regions, southwest Japan. *Journal of Geophysical Research: Solid Earth*, *117*(B6). doi: 10.1029/2011JB009083.

Shibazaki, B., & Shimamoto, T. (2007). Modelling of short-interval silent slip events in deeper subduction interfaces considering the frictional properties at the unstable—stable transition regime. *Geophysical Journal International*, *171*(1), 191–205. doi: 10.1111/j.1365-246X.2007.03434.x.

Shibazaki, B., Wallace, L. M., Kaneko, Y., Hamling, I., Ito, Y., & Matsuzawa, T. (2019). Three-dimensional modeling of spontaneous and triggered slow-slip events at the Hikurangi subduction zone, New Zealand. *Journal of Geophysical Research: Solid Earth*, *124*(12), 13250–13268. doi: 10.1029/2019JB018190.

Sibson, R. H. (1990). Conditions for fault-valve behaviour. *Geological Society, London, Special Publications*, *54*(1), 15–28. doi: 10.1144/GSL.SP.1990.054.01.02.

Sibson, R. H. (1992). Fault-valve behavior and the hydrostatic-lithostatic fluid pressure interface. *Earth-Science Reviews*, *32*(1-2), 141–144. doi: 10.1016/0012-8252(92)90019-P.

Song, T. R., Helmberger, D. V., Brudzinski, M. R., Clayton, R. W., Davis, P., Perez-Campos, X., & Singh, S. K. (2009). Subducting slab ultra-slow velocity layer coincident with silent earthquakes in southern Mexico. *Science*, *324*(5926), 502-6. doi: 10.1126/science.1167595.

Sun, T., Saffer, D., & Ellis, S. (2020). Mechanical and hydrological effects of seamount subduction on megathrust stress and slip. *Nature Geoscience*, *13*(3), 249–255. doi: 10.1038/s41561-020-0542-0.

Takagi, R., Uchida, N., & Obara, K. (2019). Along-strike variation and migration of long-term slow slip events in the western Nankai subduction zone, Japan. *Journal of Geophysical Research: Solid Earth*, *124*(4), 3853–3880. doi: 10.1029/2019JB018037.

Tan, Y. J., & Marsan, D. (2020). Connecting a broad spectrum of transient slip on the San Andreas fault. *Science advances*, *6*(33), eabb2489. doi: 10.1126/sciadv.abb2489.

Todd, E. K., & Schwartz, S. Y. (2016). Tectonic tremor along the northern Hikurangi Margin, New Zealand, between 2010 and 2015. *Journal of Geophysical*

Research: Solid Earth, *121*(12), 8706–8719. doi: 10.1002/2016JB013480.

Wallace, L. M. (2020). Slow slip events in New Zealand. *Annual Review of Earth and Planetary Sciences*, *48*, 175–203. doi: 10.1146/annurev-earth-071719-055104.

Wallace, L. M., Barnes, P., Beavan, J., Van Dissen, R., Litchfield, N., Mountjoy, J., … Pondard, N. (2012b). The kinematics of a transition from subduction to strike-slip: An example from the central New Zealand plate boundary. *Journal of Geophysical Research: Solid Earth*, *117*(B2). doi: 10.1029/2011JB008640.

Wallace, L. M., & Beavan, J. (2010). Diverse slow slip behavior at the Hikurangi subduction margin, New Zealand. *Journal of Geophysical Research: Solid Earth*, *115*, B12402. doi: 10.1029/2010JB007717.

Wallace, L. M., Beavan, J., Bannister, S., & Williams, C. (2012a). Simultaneous long-term and short-term slow slip events at the Hikurangi subduction margin, New Zealand: Implications for processes that control slow slip event occurrence, duration, and migration. *Journal of Geophysical Research: Solid Earth*, *117*, B11402. doi: 10.1029/2012JB009489.

Wallace, L. M., Beavan, J., McCaffrey, R., & Darby, D. (2004). Subduction zone coupling and tectonic block rotations in the North Island, New Zealand. *Journal of Geophysical Research: Solid Earth*, *109*, B12406. doi: 10.1029/2004JB003241.

Wallace, L. M., Hreinsdóttir, S., Ellis, S., Hamling, I., D'Anastasio, E., & Denys, P. (2018). Triggered slow slip and afterslip on the southern Hikurangi subduction zone following the Kaikōura earthquake. *Geophysical Research Letters*, *45*(10), 4710–4718. doi: 10.1002/2018GL077385.

Wallace, L. M., Kaneko, Y., Hreinsdóttir, S., Hamling, I., Peng, Z., Bartlow, N., … Fry, B. (2017). Large-scale dynamic triggering of shallow slow slip enhanced by overlying sedimentary wedge. *Nature Geoscience*, *10*(10), 765–770. doi: 10.1038/ngeo3021.

Wallace, L. M., Reyners, M., Cochran, U., Bannister, S., Barnes, P. M., Berryman, K., ... others (2009). Characterizing the seismogenic zone of a major plate boundary subduction thrust: Hikurangi Margin, New Zealand. *Geochemistry, Geophysics, Geosystems*, *10*, Q10006. doi: 10.1029/2009GC002610.

Wallace, L. M., Webb, S. C., Ito, Y., Mochizuki, K., Hino, R., Henrys, S., ... Sheehan, A. F. (2016). Slow slip near the trench at the Hikurangi subduction zone, New Zealand. *Science*, *352*(6286), 701–704. doi: 10.1126/science.aaf2349.

Wang, K., & Bilek, S. L. (2014). Fault creep caused by subduction of rough seafloor relief. *Tectonophysics*, *610*, 1–24. doi: 10.1016/j.tecto.2013.11.024.

Warren-Smith, E., Fry, B., Wallace, L., Chon, E., Henrys, S., Sheehan, A., ... Lebedev, S. (2019). Episodic stress and fluid pressure cycling in subducting oceanic crust during slow slip. *Nature Geoscience*, *12*(6), 475–481. doi: 10.1038/s41561-019-0367-x.

Watkins, W. D., Colella, H. V., Brudzinski, M. R., Richards-Dinger, K. B., & Dieterich, J. H. (2015). The role of effective normal stress, frictional properties, and convergence rates in characteristics of simulated slow slip events. *Geophysical Research Letters*, *42*(4), 1061–1067. doi: 10.1002/2014GL062794.

Wech, A., Boese, C., Stern, T., & Townend, J. (2012). Tectonic tremor and deep slow slip on the Alpine Fault. *Geophysical Research Letters*, *39*(10). doi: 10.1029/2012GL051751.

Wei, M., Kaneko, Y., Liu, Y., & McGuire, J. J. (2013). Episodic fault creep events in California controlled by shallow frictional heterogeneity. *Nature Geoscience*, *6*(7), 566–570. doi: 10.1038/ngeo1835.

Wei, M., Kaneko, Y., Shi, P., & Liu, Y. (2018). Numerical modeling of dynamically triggered shallow slow slip events in New Zealand by the 2016 M_w 7.8 Kaikoura earthquake. *Geophysical Research Letters*, *45*(10), 4764–4772. doi: 10.1029/2018GL077879.

Wei, M., McGuire, J. J., & Richardson, E. (2012). A slow slip event in the south central Alaska Subduction Zone and related seismicity anomaly. *Geophysical Research Letters*, *39*, L15309. doi: 10.1029/2012GL052351.

Williams, C. A., Eberhart-Phillips, D., Bannister, S., Barker, D. H., Henrys, S., Reyners, M., & Sutherland, R. (2013). Revised interface geometry for the Hikurangi subduction zone, New Zealand. *Seismological Research Letters*, *84*(6), 1066–1073. doi: 10.1785/0220130035.

Zal, H. J., Jacobs, K., Savage, M. K., Yarce, J., Mroczek, S., Graham, K., ... Henrys, S. (2020). Temporal and spatial variations in seismic anisotropy and V_p/V_s ratios in a region of slow slip. *Earth and Planetary Science Letters*, *532*, 115970. doi: 10.1016/j.epsl.2019.115970.

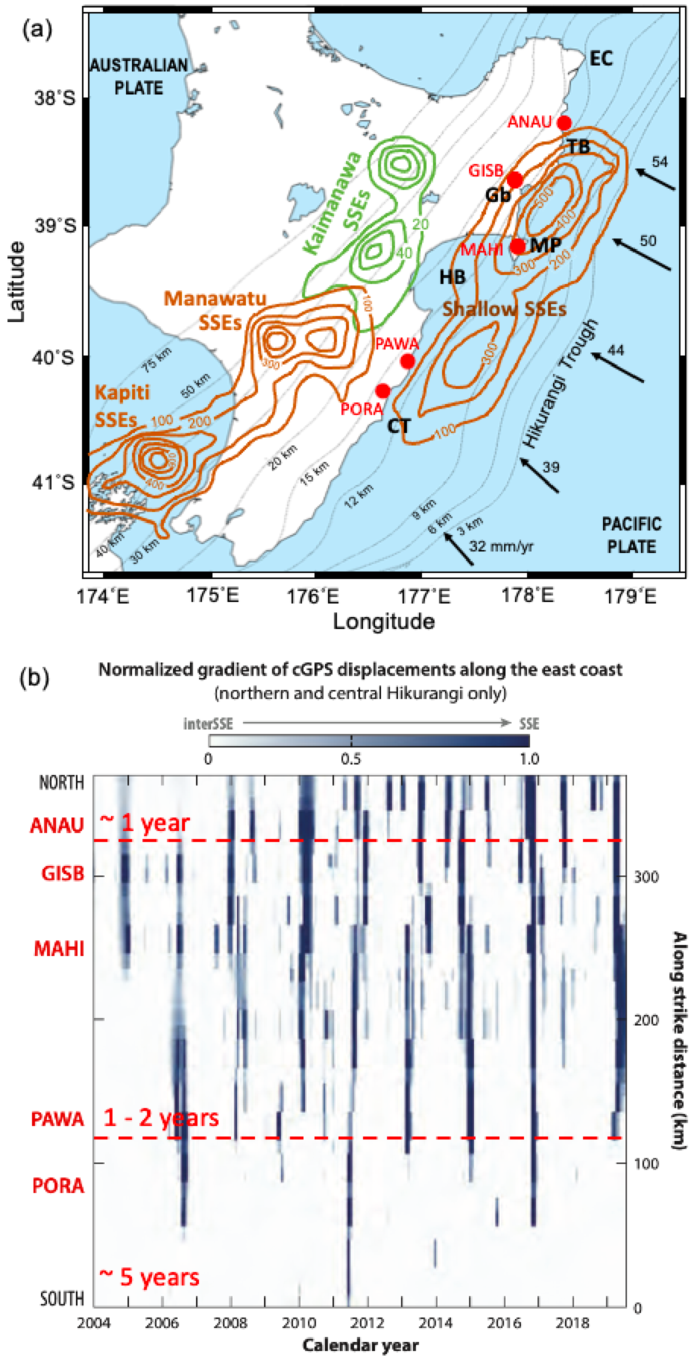

Figure 1. (a) Cumulative slow slip in the North Island of New Zealand for the 2002 - 2014 period (contours from Fig. 1 in Wallace, 2020). Brown contours are 100-mm slip contour intervals. Green contours show 20-mm slip intervals. Red dots show the location of continuous GPS (cGPS) stations ANAU, GISB, MAHI, PAWA and PORA, labeled in (b). Black arrows indicate the plate convergence rate in mm/year (data from Wallace et al., 2012b). Thin black lines are the depth contour (below sea level) of the subducting plate interface (based on Williams et al., 2013). Abbreviations: EC, East Cape; TB, Tolaga Bay; Gb, Gisborne; MP, Mahia Peninsula; HB, Hawkes Bay; CT, Cape Turnagain. (b) Change in rate of motion of GeoNet cGPS stations as a normalized gradient. Darker colors represent fastest rate change, indicative of slow slip events (SSEs). White color indicate inter SSE velocities. The time series are projected along-strike (y-axis). Red labels on y-axis indicate the location of the cGPS stations shown in (a). Dashed red lines divide the along-strike distance into three segments based on the change in the recurrence interval of SSEs. The estimated recurrence interval at each segment is shown in red. Figure modified from Wallace (2020)

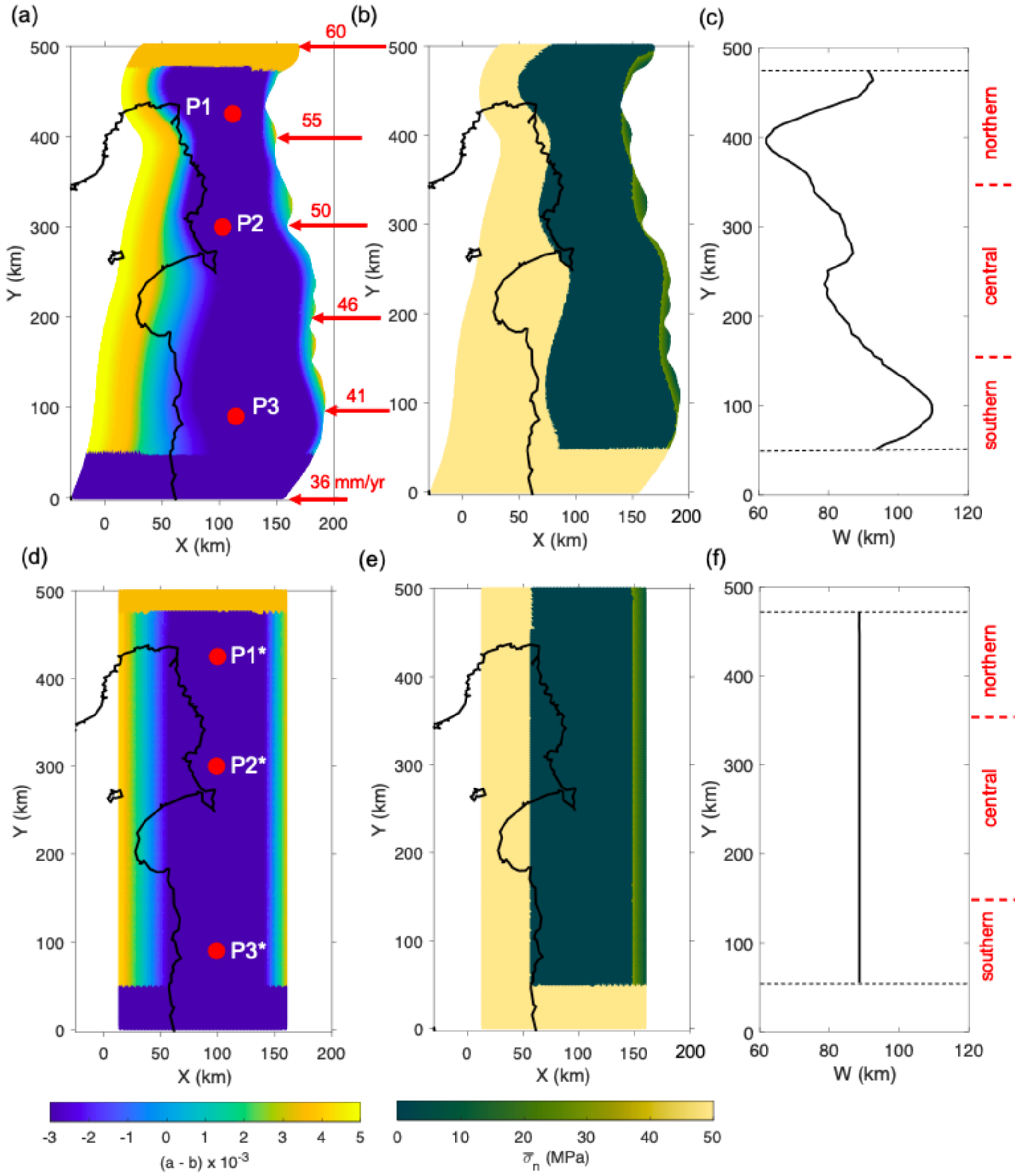

Figure 2. Model setup of (a-c) non-planar and (d-f) planar geometries with the map view distribution of (a,d) friction parameter $(a - b)$ and (b,e) $\bar{\sigma}_n$ on the fault. Note that while the model with $(a - b)$ = -0.003 and $\bar{\sigma}_n$ = 1 MPa in the SSE zone is shown in this Figure, we also consider the case with ($a - b$) = -0.0003 and $\bar{\sigma}_n$ = 10 MPa. Red arrows in (a) indicate the plate convergence rate along-strike in mm/yr. Along-strike variation of W for (c) non-planar and (f) planar geometry. Dashed lines in (c) and (f) mark the along-strike limit of the SSE zone. Red labels on the right indicate three segments into which the fault geometry is divided: northern (350 km<Y <475 km), central (150 km<Y<350 km) and southern (50 km<Y<150 km). P1-P3 and P1* - P3* are reference points.

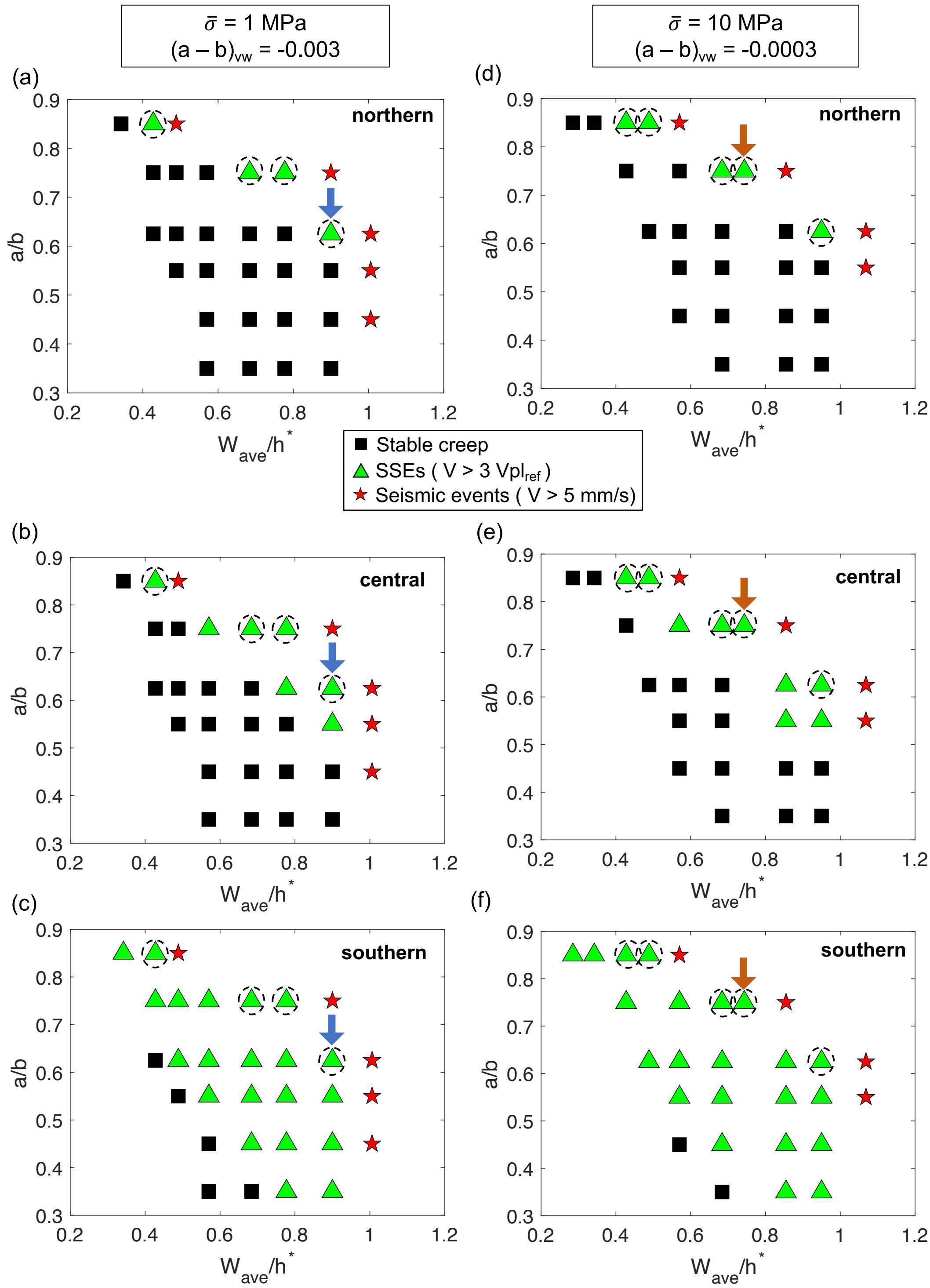

Figure 3. Simulated slip patterns (stable creep, SSEs or seismic events) for different combinations of a/b and W_{ave}/h^* parameters. W_{ave}=87.5 km is the average W along-strike from Figure 2c. Northern (a,d), central (b,e) and southern (c,f) correspond to the segments defined along the strike of the fault (Figure 2). (a - c) Simulation cases with $\bar{\sigma}_n$ = 1 MPa and $(a-b)$ = -0.003, and (d - f) with $\bar{\sigma}_n$ = 10 MPa and $(a-b)$ = -0.0003. Blue arrow indicates the preferred model. Orange arrow is the best model for $\bar{\sigma}_n$ = 10 MPa. Dashed circles highlight simulation cases where SSEs emerge in all three segments. All simulations were carried out assuming the W distribution along-strike shown in Figure 2c.

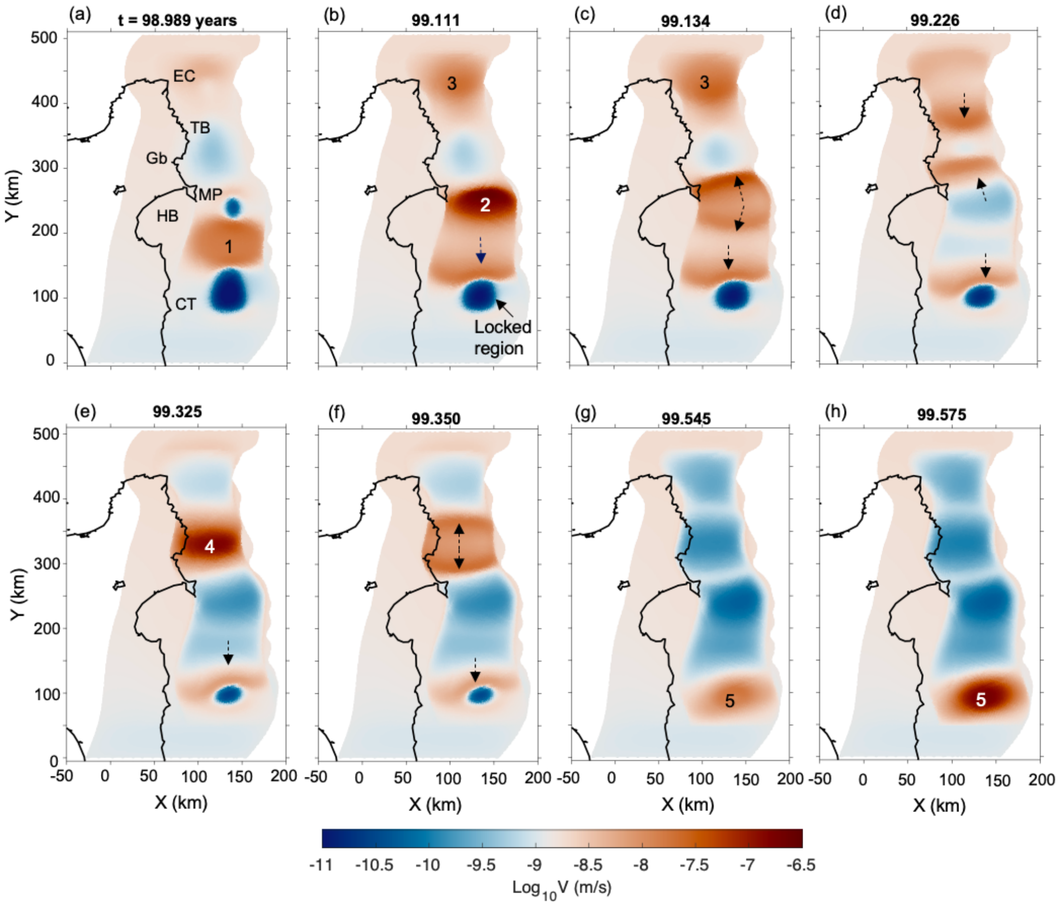

Figure 4. Snapshots of the slip velocity on the fault at eight successive time steps. Bold number on top of each figure indicates the simulation time in years. The lightest brown colors indicate regions that slide close to the plate convergence rate; dark blue corresponds to locked portions of the fault, that slip at 1 to 2 orders of magnitude below the plate rate, and brown to dark brown colors are indicative of SSEs, which emerge spontaneously as patches of high velocities. SSEs are numbered from 1 to 5 in order of their occurrence. Dashed arrows indicate migration of SSEs. Abbreviations indicate reference locations: EC, East Cape; TB, Tolaga Bay; Gb, Gisborne; MP, Mahia Peninsula; HB, Hawke Bay and CT, Cape Turnagain.

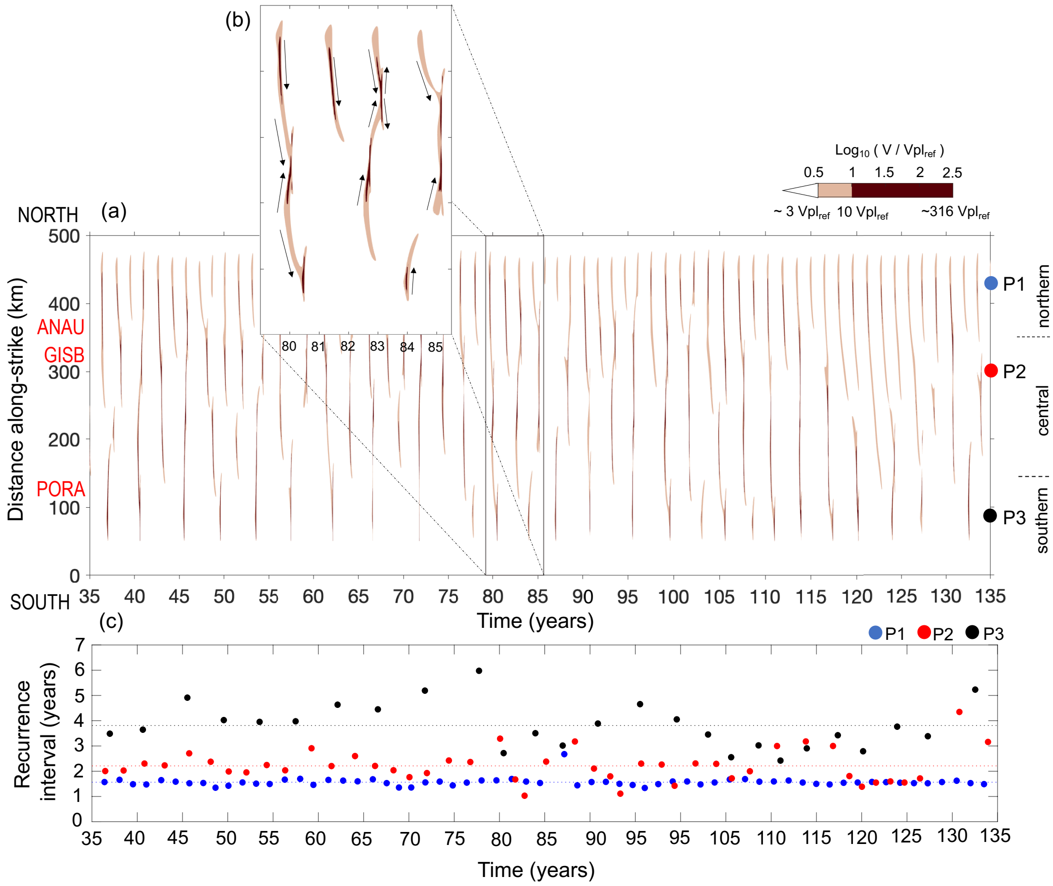

Figure 5. (a) Slip velocity evolution along the margin, in $\log_{10}$ V/Vpl$_{ref}$ scale, at 10 km depth. Slip velocities larger than V > $10^{0.5}$ Vpl$_{ref}$ (~3 Vpl$_{ref}$ or 0.39 mm/day) are plotted here. The entire range of slip velocities is shown in Figure S3. Red labels show along-strike locations of some reference cGPS stations (see Figure 1 for location in map view). Colored circles indicate the along-strike location of points P1, P2 and P3 shown in Figure 2a. Northern, central and southern indicate the three segments intro which the along-strike distance is divided (Figure 2). (b) Zoom in of 6.5 years. Dark arrows indicate the along-strike migration of slip fronts. (c) Recurrence interval of SSEs (brown contours in (a)) at points P1, P2 and P3.

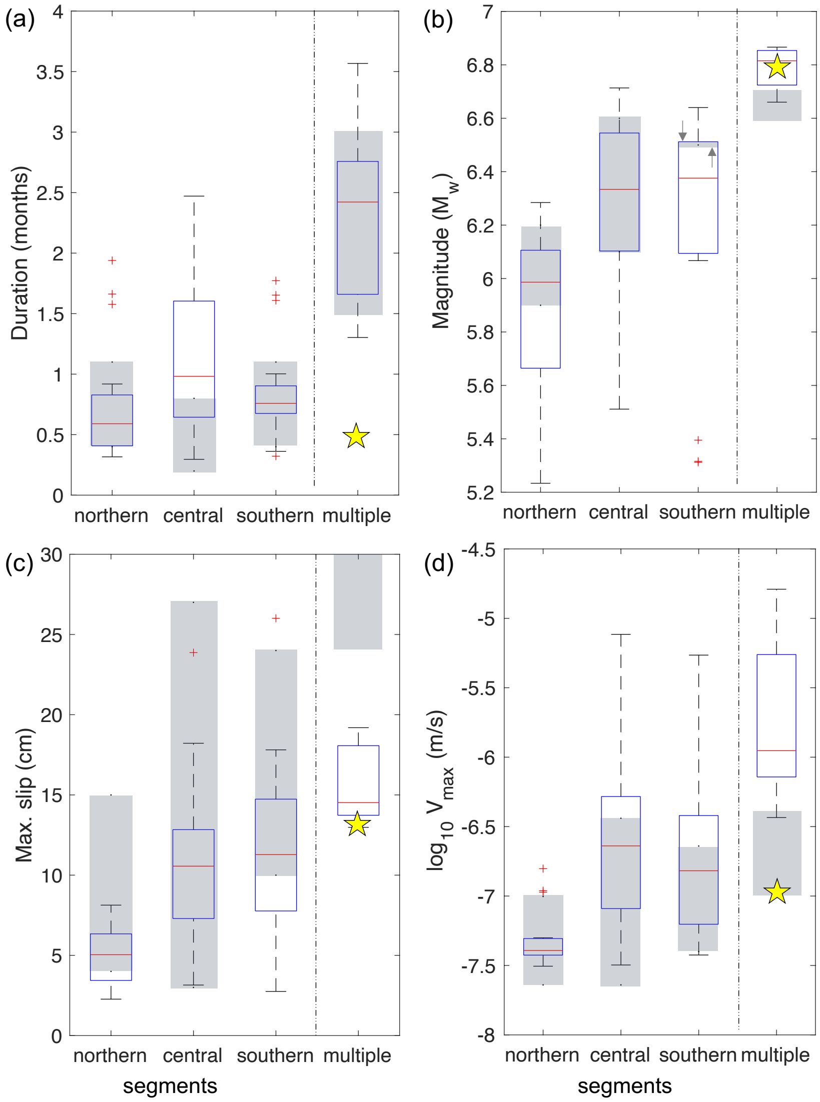

Figure 6. Modeled (box plot) and observed (gray-shaded bars) source properties of SSEs that emerge at the northern, central and southern segments (Figure 2). 'Multiple' refers to multi-segment SSEs. Gray-shaded bars indicate the observed ranges of SSEs taken from the catalog in Ikari et al. (2020). According to the location of observed SSEs, we classified them into different segments. SSEs emerging offshore Tolaga Bay or North of Gisborne, were included in the northern segment; SSEs offshore Giborne, Mahia Peninsula or Hawke's bay, in the central; and SSEs offshore Cape Turnagain in the southern. To constrain the range of multisegment SSEs, we consider the 2006 and 2011 SSE sequences, each one composed of several smaller SSEs that ruptured different segments along the margin, as single SSEs. We then added up the moment and max. slip of the smaller SSEs of each sequence, while the max. slip rate corresponded to the largest velocity reached in each sequence. (a) Duration, (b) Magnitude, (c) Maximum slip and (d) Maximum slip rate are shown. Double arrows in (c) highlight the location of the observed range (gray-shaded bar) in the southern segment. Blue box shows 50% of the simulated SSE source properties, from the 25th to the 75th percentile. Red line within the box corresponds to the median value. Dashed black line are the whiskers of the box, which cover ±2.7 times the standard deviation. Outliers are shown as red crosses. Yellow stars indicate the source properties of the 2016 East Coast SSE that was triggered by the Kaikoura earthquake's seismic waves (Wallace et al., 2018).

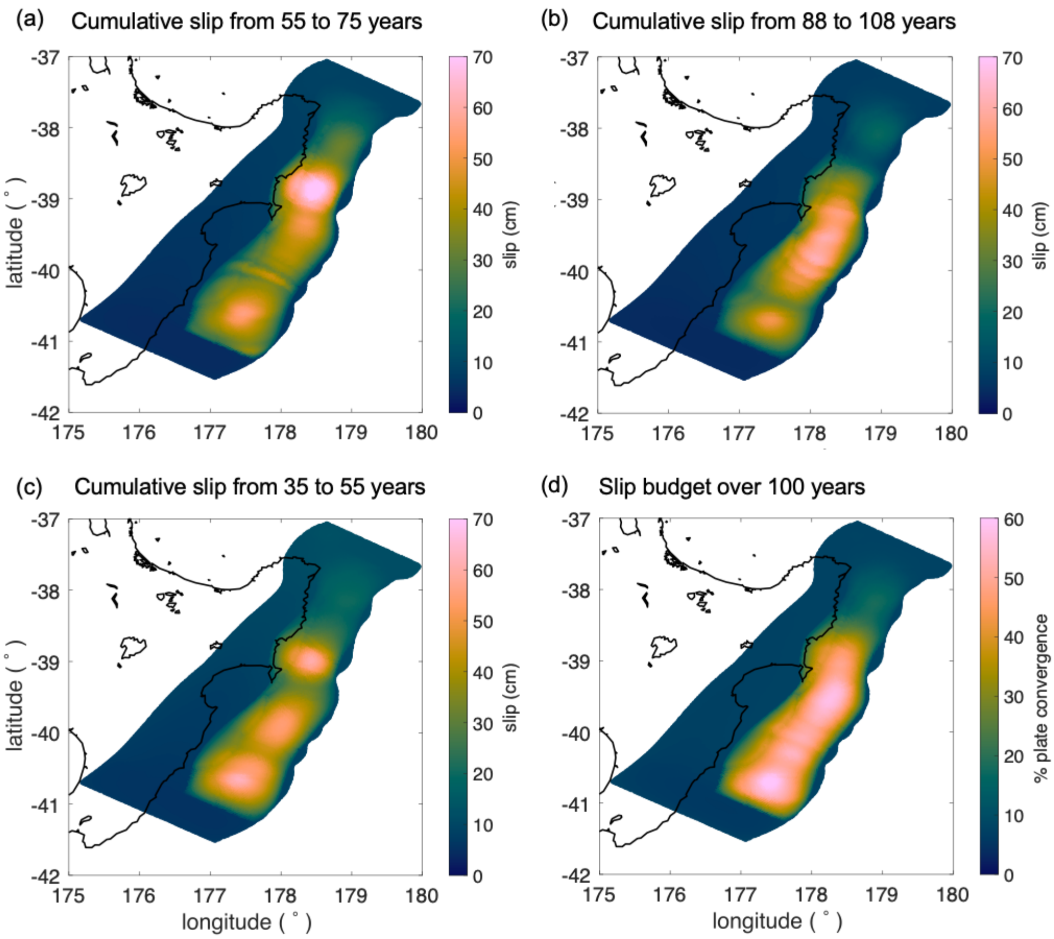

Figure 7. Cumulative slip of SSEs emerging in the preferred model from (a) 55 to 75 years, (b) 88 to 108 years and (c) 35 to 55 years. (d) Slip released by SSEs over 100 years as a percentage of the plate convergence rate.

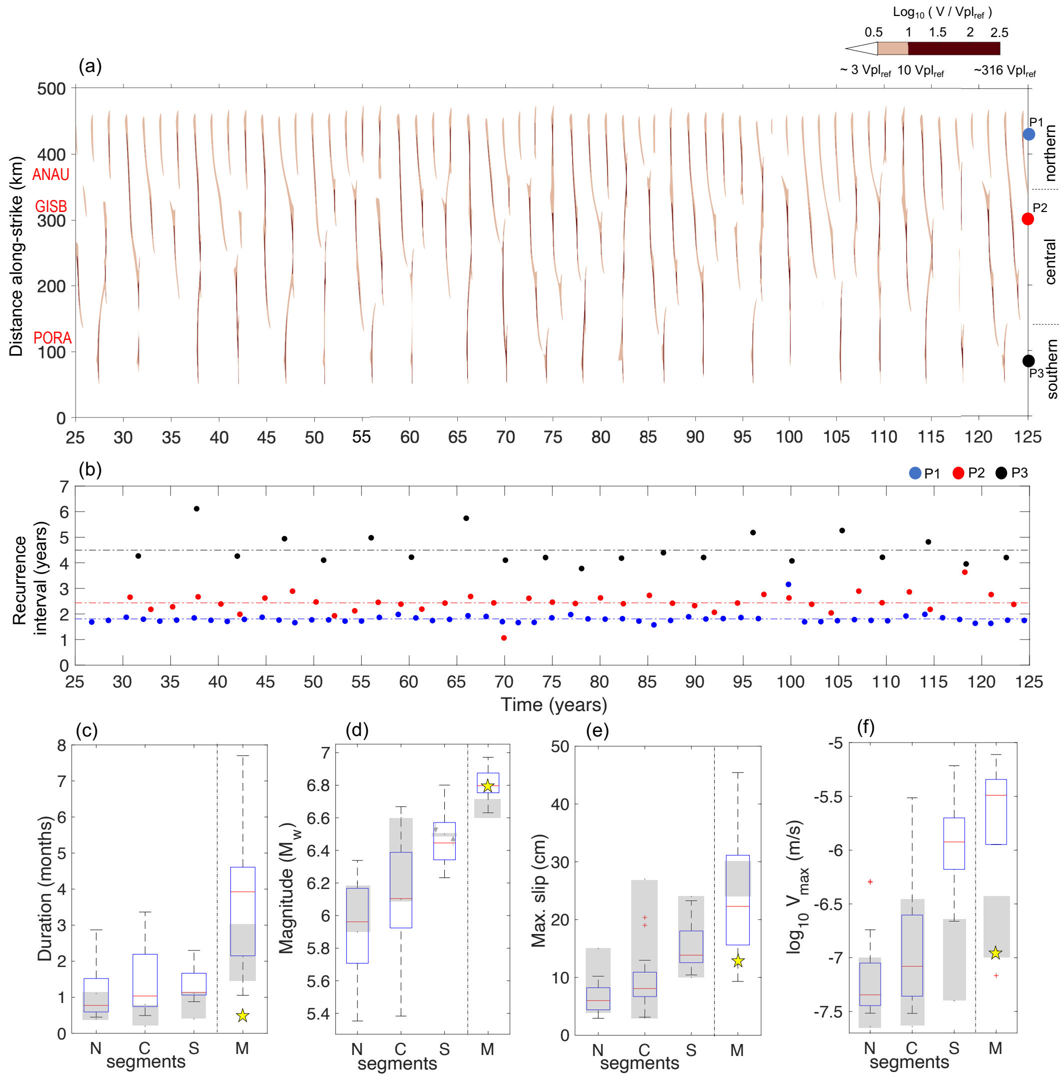

Figure 8. Best fit model for $\bar{\sigma}_n$ = 10 MPa and $(a - b)$ = -0.0003 in the SSE zone. (a) Slip velocity evolution along the margin, in $\log_{10}$ V/Vpl$_{\mathrm{ref}}$ scale, at 10 km depth. Slip velocities larger than $10^{0.5}$ Vpl$_{\mathrm{ref}}$ ($\sim$3 Vpl$_{\mathrm{ref}}$ or 0.39 mm/day) are plotted here. (b) Recurrence interval of SSEs at points P1, P2 and P3 (colored circles in (a), see map view location in Figure 2a). (c-f) Box plot shows the distribution of source properties of modeled SSEs at each segment. N, C and S, stand for the northern, central and southern segments, respectively. M denotes multisegment SSEs. Description of box plot is the same as in Figure 6. Gray-shaded bars indicate observed ranges for SSEs' source properties, taken from Ikari et al. (2020) catalog.

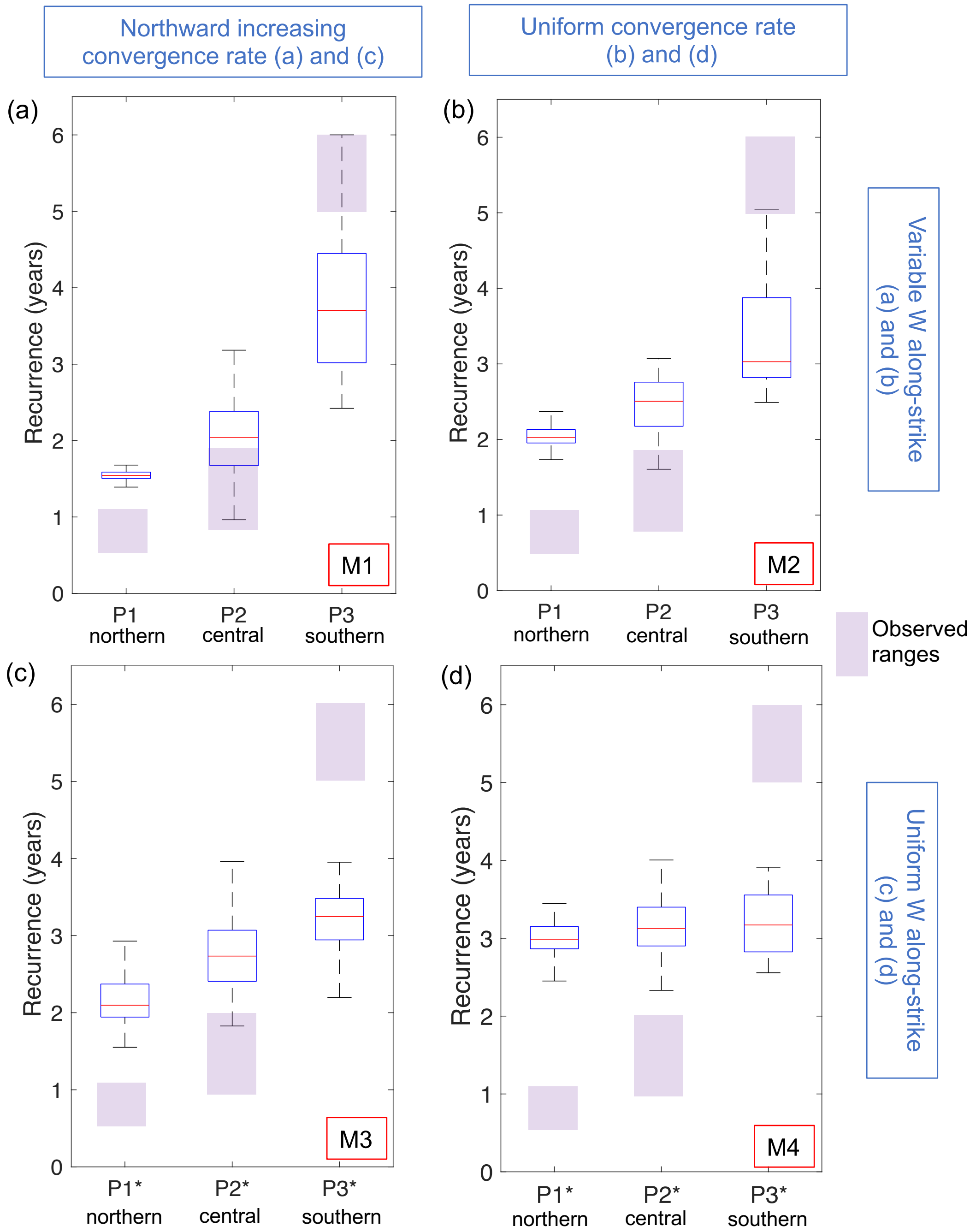

Figure 9. Recurrence interval of modeled SSEs at three points along the margin, P1$^{(*)}$ to P3$^{(*)}$ (see Figure 2a and 2d for location of points) over a 100-year period. Northern, central and southern correspond to the segments where each point is located. Purple-shaded bars show the observed recurrence interval of SSEs estimated from Figure 1b. M1 corresponds to the preferred model described in section 3.2. M2 to M4 are additional models described in section 3.3. Model setup with (a,b) non-planar geometry and variable W along-strike (Figure 2c), and with (c,d) planar geometry and uniform W along-strike (Figure 2f). Simulations with (a,c) variable and (b,d) uniform plate convergence rate along-strike. Box plots show the distribution of the recurrence intervals at each point. Blue box shows the distribution of 50% of the recurrence intervals, from the 25th to the 75th percentile. Red line within the box corresponds to the median value. Dashed black line are the whiskers of the box, which cover ±2.7 times the standard deviation. Outliers are not shown in this Figure.

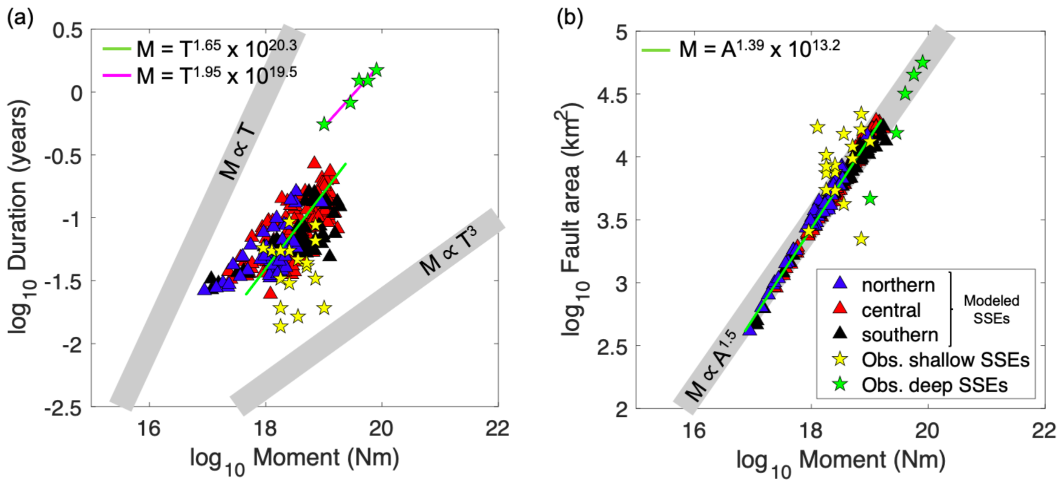

Figure 10. Comparison of scaling properties between observed (stars) and modeled (triangles) SSEs along the Hikurangi margin. Modeled SSEs are classified according to the segment: northern (blue), central (red) and southern (black). Source properties of observed SSEs (taken from Ikari et al. (2020) catalog) are classified into shallow (yellow stars) and deep (green stars) SSEs. (a) Moment-duration scaling relation. Green line shows the best fit line for the modeled SSEs with $M = T^{1.65} \times 10^{20.3}$. $M \propto T$ and $M \propto T^3$ scalings are shown as reference. Magenta line shows the best fit line for observed deep SSEs with $M = T^{1.95} \times 10^{19.5}$. (b) Moment-area scaling relations. Green line shows the best fit line for the modeled SSEs with $M = A^{1.39} \times 10^{13.2}$. $M \propto A^{1.5}$ is shown as reference.

Table 1. List of parameters for preferred model assuming $\bar{\sigma}_n = 1$ MPa or 10 MPa in the SSE zone.

Definition	Parameter	Value
Nucleation size	h^*	95 km (115 km)*
Characteristic slip distance	d_c	8.39 mm (6.77 mm)
Effective normal stress in the SSE zone	$\bar{\sigma}_n$	1 MPa (10 MPa)
Friction parameter	$a - b$	-0.003 (-0.0003)
Direct effect	a	0.005 (0.0009)
Shear modulus	μ	15 GPa
Poisson's ratio	ν	0.25
Steady state friction coefficient at V_o	f_o	0.6

*Values in parentheses are for best-fitted model assuming $\bar{\sigma}_n = 10$ MPa in the SSE zone only.

Supporting Information for "Segmentation of shallow slow slip events at the Hikurangi subduction zone explained by along-strike changes in the fault geometry and plate convergence rates"

Andrea Perez-Silva[1], Yoshihiro Kaneko[2], Martha Savage[1], Laura Wallace[3,4],

Duo Li[5], Charles Williams[3]

[1]School of Geography, Environment and Earth Sciences, Victoria University of Wellington, PO Box 600, Wellington 6140, New Zealand.

[2]Department of Geophysics, Kyoto University, Sakyo-ku, Kyoto 606-8501, Japan.

[3]GNS Science, PO Box 30368, Lower Hutt 5011, New Zealand.

[4]Institute for Geophysics, University of Texas at Austin, Austin, TX, USA.

[5]Department of Earth and Environmental Sciences, Ludwig-Maximilians-University Munich, Theresienstrasse 41, 80333 Munich, Germany.

Contents of this file

1. Text S1 to S3
2. Captions for Movie S1 and S2
3. Figures S1 to S9
4. Tables S1 to S2

Additional Supporting Information (Files uploaded separately)

---

1. Movie S1 and S2

Text S1: Governing equations The quasi-dynamic formulation describes the relation between the stress and the slip history on the fault (Rice, 1993). This formulation is an approximation of the fully dynamic equations, in that it does not account for the full inertial (wave) effects, i.e. for the stress changes due to wave propagation (Rice, 1993). Instead, these changes are approximated by a radiation damping term, that represents the final static stress changes as predicted by the exact solution of the full elastodynamic equations (Rice, 1993). The spatial and temporal discretization of this formulation is given by:

$$\tau_i(t) = -\sum_{j=1}^{N} K_{i,j}(\delta_j(t) - V_{pl}t) - \eta \frac{d\delta_i(t)}{dt} \ , \tag{1}$$

where t is the time step and the subscripts i, j are associated with an individual cell. τ_i and δ_i are shear stress and slip at element i, respectively. V_{pl} is the plate convergence rate, which in our model setup increases along the fault strike from 36 to 60 mm/yr (Figure S1). The term η represents the radiation damping factor, defined as $\eta = \frac{\mu}{c_s}$, where μ is the elastic shear modulus and c_s is the shear wave speed. The stiffness matrix or Green's function, $K_{i,j}$, describes the change in shear stress on element i due to a unit dislocation in the dip direction on element j. K_{ij} is calculated in an elastic half-space medium and adapted to triangular dislocation elements by Stuart, Hildenbrand, and Simpson (1997).

The code incorporates rate- and state-dependent frictional (RSF) laws (Dieterich, 1979), in which the shear strength, τ, is described as a logarithmic function of the slip rate V and a state variable θ, which represents the temporal state of the asperity contacts and time dependent processes (Blanpied et al., 1998). The constitutive law follows the equation:

$$\tau = \bar{\sigma} f = \bar{\sigma}[f_0 + a \ln\left(\frac{V}{V_0}\right) + b \ln\left(\frac{V_0\theta}{d_c}\right)], \tag{2}$$

where f refers to the instantaneous friction coefficient, f_0 is the steady state friction coefficient at reference rate V_0 and d_c is the characteristic slip for state evolution. $\bar{\sigma}$ is the effective normal stress, defined as the difference between the lithostatic stress and pore fluid fluid pressure ($\bar{\sigma}$ = σ - p). $a > 0$ and $b > 0$ are constitutive parameters that represent the instantaneous change of friction due to a sudden change in velocity and the evolution of friction with slip distance, respectively (Dieterich, 1979). Parameter $(a - b)$ determines the frictional stability regime of the fault, when $(a - b) > 0$, steady-state friction $f_{\rm ss}$ increases with velocity, known as steady-state velocity-strengthening (VS). In a VS regime, slip is always stable. A steady-state velocity-weakening (VW) regime occurs when $(a - b) < 0$. In this regime, slip could be unstable (seismic) or conditionally stable (Scholz, 1998). Parameter $(a - b)$ depends on the temperature, the rock type and the effective normal stress (Marone et al., 1990; Blanpied et al., 1998).

In our model, the evolution of the state variable is described by the Dietrich or 'aging' law, which assumes that the state variable and friction evolve during stationary contacts (Dieterich, 1979):

$$\frac{d\theta}{dt} = 1 - \frac{V\theta}{d_c}. \tag{3}$$

At steady state, the state variable can be interpreted as the lifetime of contact areas (d_c/V_0), assuming that d_c is a typical contact size (Ampuero & Rubin, 2008).

Other formulations of the evolution of the state variable have been proposed. In the Ruina or 'slip law', the evolution of the state variable always involves slip, even during stationary contacts

(Marone et al., 1990). Composite laws, that combine several versions of RSF law, have also been proposed (Kato & Tullis, 2001). The formulation that best describes a range of laboratory experiments remains a subject of ongoing research (Bhattacharya et al., 2017; Kaneko et al., 2016).

A theoretical estimate of the upper bound of a critical nucleation size is given by Rubin and Ampuero (2005):

$$h^* = \frac{2\mu b d_c}{\pi(1-\nu)(b-a)^2\bar{\sigma}}, \tag{4}$$

where μ and ν are the shear modulus and the Poisson ratio, respectively. d_c is the characteristic slip distance, $\bar{\sigma}$ the effective normal stress and $(b-a)$ is the average value of the friction parameter in the region under VW conditions. In this study, we assume $\mu = 15$ GPa and $\nu = 0.25$.

Text S2: Alternative model setups. Apart from the model setup presented in the main text, we consider three alternative setups (A, B and C) to examine the consequence of some of our modeling assumptions. To assess the fitness of each alternative setup, we compare the source properties of simulated SSEs with observations, following the same approach describe in the main text (Section 3.2.2). Note that unless otherwise stated, the model parameters for the three alternative models are the same as in the preferred model (Table 1).

Alternative Model A: In this model, we consider the case of an SSE zone extending all the way to the trench, at 2.5 km depth below sea level. This setup differs from the preferred model, where the SSE zone starts at 4 km depth, and was motivated by the lack of constraints on the updip limit of slip of SSEs. To keep the value of h^* as in the preferred model, we slightly move the downdip limit of the SSE zone upwards. The slip rate evolution along depth (at Y = 103 km) for Alternative Model A and the preferred model are shown in Figure S6. In Model A, during SSE episodes, larger slip rates (V > 10 $\mathrm{Vpl_{ref}}$) extend all the way to the trench (brown contours in Figure S6d), whereas in the preferred model, slip rates in the trench region increase only up to the plate convergence rate during SSEs (beige contours in Figure S6b). In contrast, the slip rate evolution along-strike (Figure S5a) is similar to that in the preferred model (Figure S3). Model A reproduces the along-strike segmentation of SSEs (Figure S5b), as well as their source properties (Figure S5c). Based on these results, we cannot rule out that observed SSEs could also extend all the way to the trench.

Alternative Model B: To better enforce the strong coupling inferred in the southern part of the margin (Wallace & Beavan, 2010), in this model we assume a different parameter setting in this region. Following a similar approach to Liu and Rice (2007), we reduce the value of d_c in the region from 0 to 50 km along-strike, such that h^* is the same in the coupled region as in the SSE zone (i.e. 95 km). We find that this new setup leads to slip velocities of at least one order of magnitude lower than $\mathrm{Vpl}_{\mathrm{ref}}$ for 0 km $<$ Y $<$ 50 km, as shown in Figure S7a. Over time the region gradually unlocks; for instance at 110 years the plate slides close to the plate convergence rate between 0 km to 25 km along-strike (Figure S7a). This model setup captures the along-strike segmentation in the recurrence interval of shallow SSEs (Figure S7b), as well as their source properties (Figure S7c to S7e), which indicates that the locking condition does not significantly affect the model results.

Alternative Model C: In this case we do not consider the VW and VS bands on both ends of the model geometry, from 0 km $<$ Y $<$ 50 km and 475 km $<$ Y $<$ 500 km, respectively. Instead, we assume that the SSE zone also extends across these regions. This setup was motivated to determine whether the segmentation of SSEs depended on the specific parametrizations of these regions. The slip rate evolution along-strike (Figure S8a) indicates that assuming this model setup, SSEs extend across the entire model geometry along-strike (from 0 $<$ Y $<$ 500 km) within the SSE zone. This contrasts with the preferred model, where SSEs extend from $50 < Y < 475$ km. At the same time, we find that, despite the longer spatial extent of SSEs due to the larger SSE zone, the recurrence interval of these SSEs is still segmented along-strike (Figure S8b), which indicates that the slip behavior on the boundaries of the preferred model does not affect the segmentation of these events.

Text S3: Planar fault geometry

In section 3.3, we consider a planar fault to investigate the importance of non-planar fault geometry on the segmentation of modeled SSEs. The planar fault geometry has the same along-strike length and depth range as the non-planar geometry does, with the difference that the fault dip angle is constant ($\alpha = 7$ °). We discretize the planar fault by 21607 triangular elements using Trellis software, each triangle has an area of ∼3.9 km^2 and a side length (dx) of ∼3 km. In this case, we assume a larger cell size than in the non-planar geometry to reduce computational costs, however, this difference does not affect the numerical resolution of the model, as we ensure that h^* is well resolved. In this setup $h^* = 115$ km, thus $h^*/dx > 30$, which is larger than the ratio assumed by Liu and Rice (2005) in their planar fault model, where $4 < h^*/dx < 8$.

Movie S1: Slip rate evolution on the fault over several SSE cycles: The movie shows the slip velocity on the fault over the time interval shown in the snapshots of Figure 4. See Section 3.2.1 for a description of the slip rate evolution.

Movie S2: Slip rate evolution during a multisegment SSE. The movie shows an example of a multisegment SSE that ruptures the southern and central part of the fault. The event nucleates in the southern part of the margin (offshore Cape Turnagain) and splits into two divergent slip fronts. The northward-propagating slip front migrates at a speed of ∼2.4 km/day. When approaching Mahia Peninsula the SSE reaches the maximum slip velocity, V_{max} ∼10^{-6}

m/s. Afterwards, it splits again into two divergent slip fronts. We note that this event was considered a single event, instead of two consecutive ones, because the slip velocity exceeds the velocity threshold of 20 Vpl_{ref} over the total duration of the event.

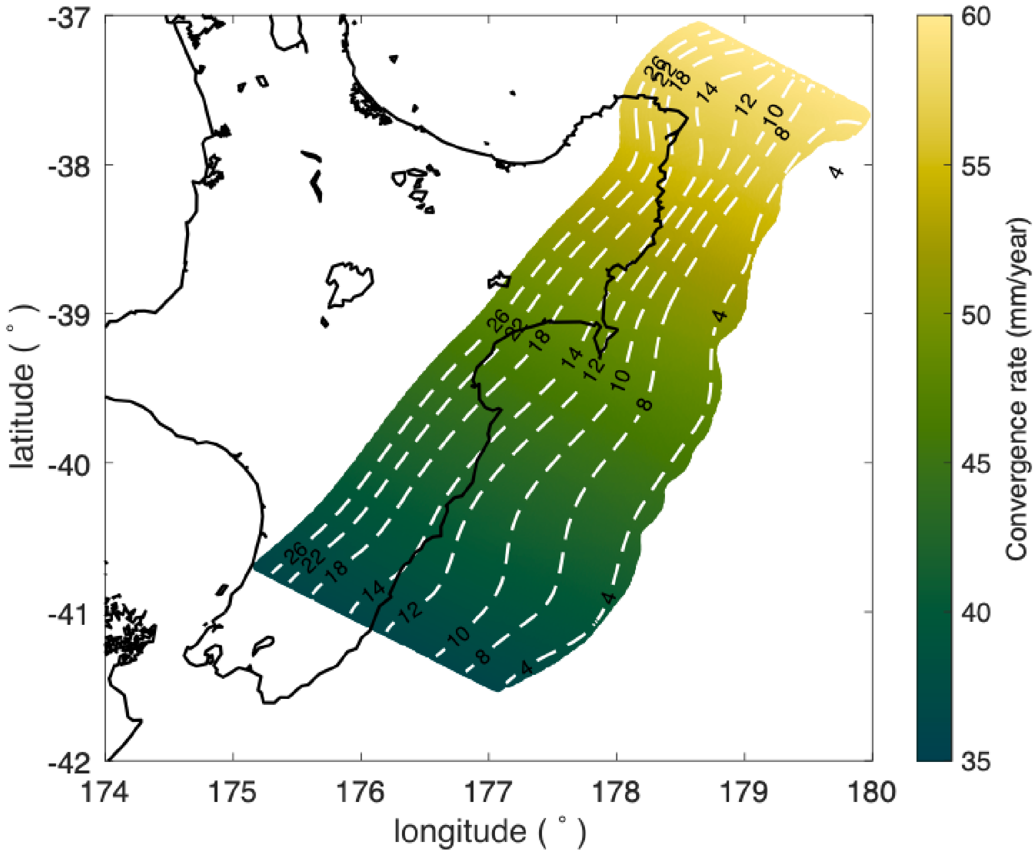

Figure S1. 3D non-planar geometry of the Hikurangi plate interface based on Williams et al. (2013). Dashed white lines represent isodepth contours in km. The plate convergence rate increases from 36 to 60 mm/yr along the strike of the model geometry, following the estimates in Wallace et al. (2004).

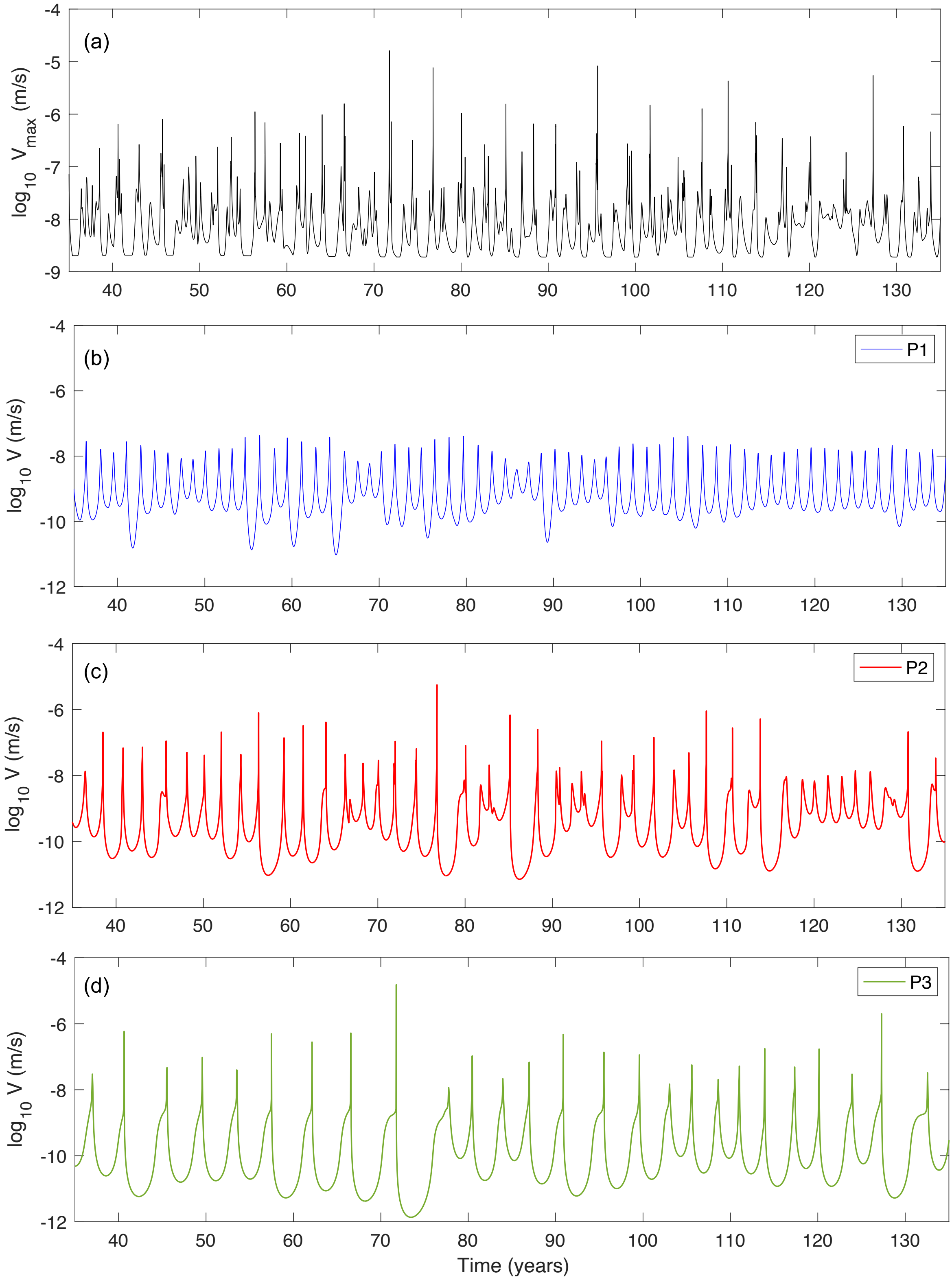

Figure S2. Slip rate during a 100-year simulation period from preferred model. Maximum slip rate along the fault (a). Slip rate at points P1 (b), P2 (c) and P3 (d) (located in Figure 2a). Peak slip velocities, as well as the time interval between peak velocities, increase from P1 to P3.

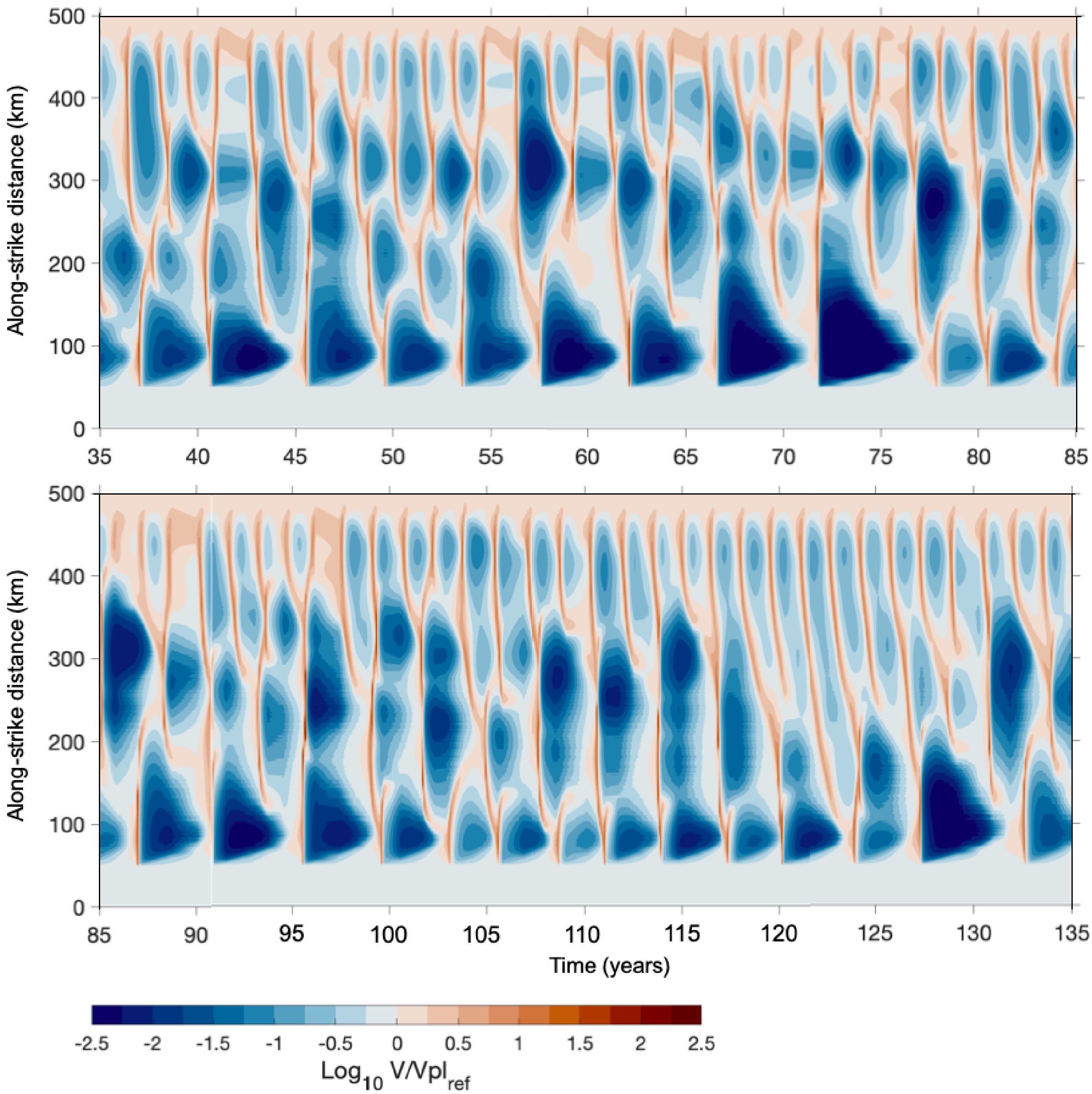

Figure S3. Evolution of slip velocity along strike, in $\log_{10}$ (V/Vpl_{ref}) scale, at 10 km depth. Results correspond to the preferred model.

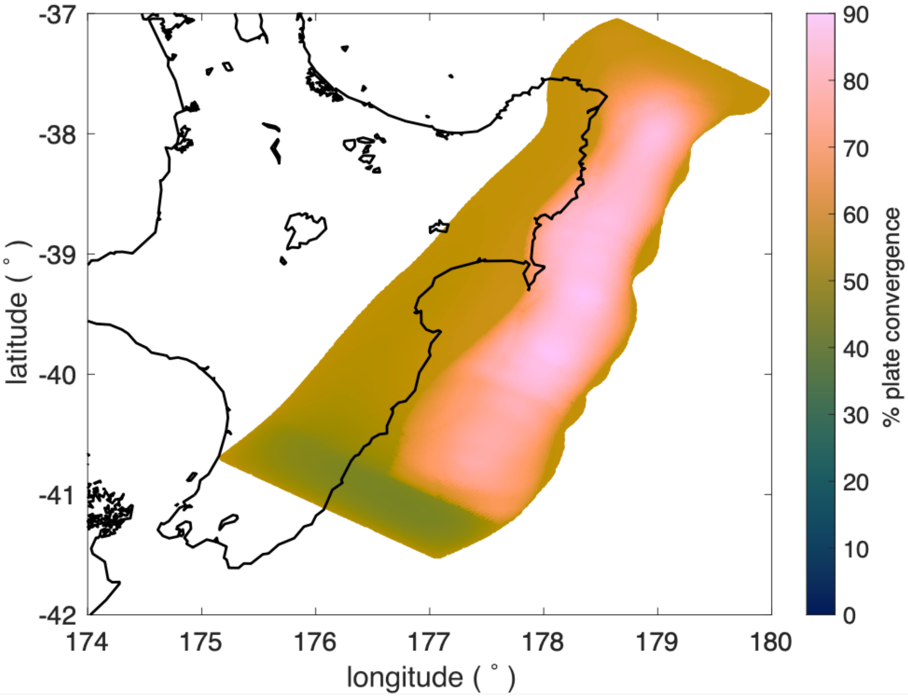

Figure S4. Slip released by SSEs over 100 years as a percentage of the plate convergence rate assuming a slip threshold of 3 Vpl_{ref} to define an SSE. Results correspond to the preferred model.

Table S1. Summary of alternative model setups (A, B, C) described in Text S2.

Alternative model setups	Model setup*	Model results*
Model A (Figs. S5, S6)	The SSE zone extends all the way to the trench at 2.5 km depth below sea level	Larger slip velocities ($V > 10$ Vpl_{ref}) reach the trench
Model B (Fig. S7)	Different parameter setting in the southern part of the margin (for 0 km<Y <50 km) to better enforce the strongly locked coupling	The plate slides up to one order of magnitude below the plate rate in the southern part of the margin (0 <Y <50 km)
Model C (Fig. S8)	No VW nor VS bands at the ends of the model geometry along-strike	SSEs extend along the entire fault along-strike (500 km)

* We only describe the differences with respect to the preferred model in the main text (M1).

Table S2. Description of models M1-M4 presented in Section 3.3.

Models	Fault geometry	Model parameters	W along the fault strike	Plate rate (Vpl) along the fault strike
M1 (preferred, Figs. 4-7, 9a, 10)	Non-planar	Given in Table 1.1. $\bar{\sigma}$ and (a-b) distribution given in Figs 2a to 2b	W varies along-strike (Figure 2c)	Vpl increases northward along-strike (Figure S1)
M2 (Fig. 9b)	Non-planar	Same as M1	Same as M1	Vpl = 45 mm/yr everywhere
M3 (Fig. 9c)	Planar	Given in Table 1.1, except that dc = 10.2 mm and h* = 115 km. $\bar{\sigma}$ and (a-b) distribution given in Figures 2d to 2e	W is uniform along-strike	Vpl increases northward along-strike
M4 (Fig. 9d)	Planar	Same as M3	Same as M3	Vpl = 45 mm/yr everywhere

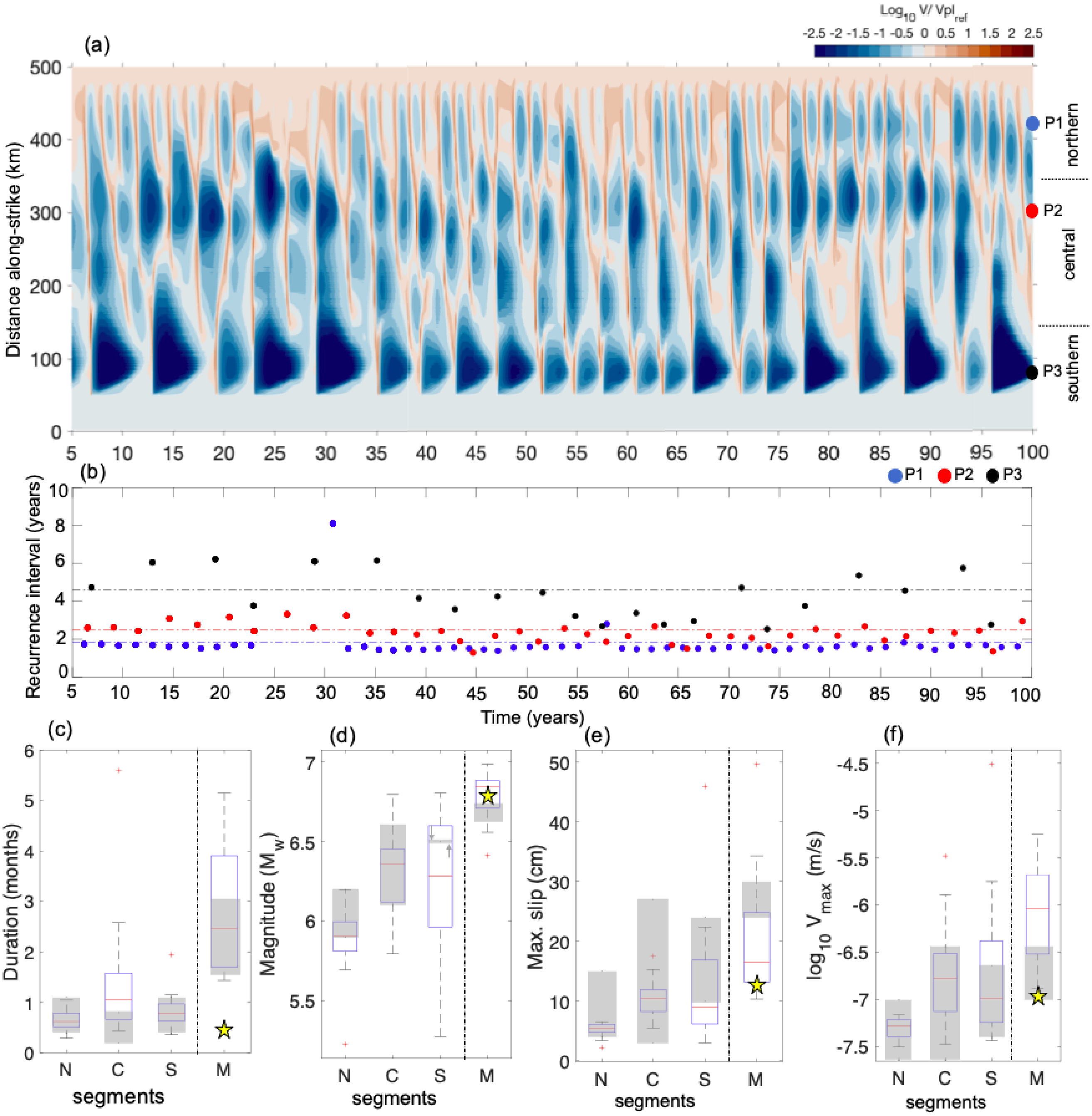

Figure S5. Results for *Model A*. Simulation case with SSE zone starting from the trench at 2.5 km depth. (a) Slip rate along-strike, in $\log_{10}$ V/Vpl$_{\mathrm{ref}}$, at 10 km depth. (b) Recurrence interval of slow slip episodes at points P1, P2 and P3 (colored circles in item (a), see map view location in Figure 2a). (c-f) Box plot show the distribution of source properties of modeled SSEs at each segment. N, C, S correspond to northern, central and southern segments. M denotes multisegment SSEs. Gray bars indicate observed ranges for SSEs' source properties taken from Ikari et al. (2020) catalog. Box plot description is the same as for Figure 6 in the main text.

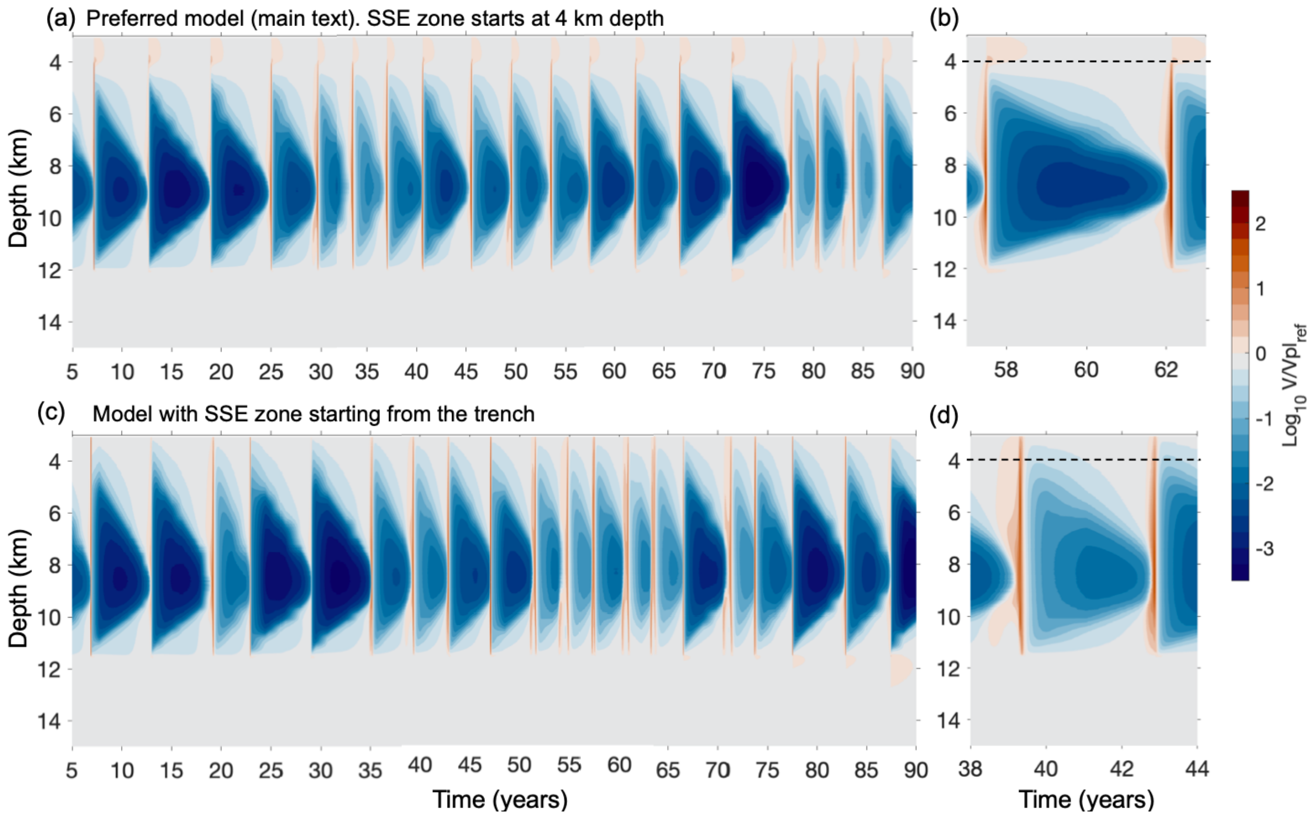

Figure S6. Slip rate evolution along depth at Y = 103 km for (a) Preferred model with SSE zone starting from 4 km depth. (b) Zoom in over six years from item (a). Dashed line highlights 4 km depth. (c) Model B with SSE zone starting from the trench, at 2.5 km depth. (d) Zoom in over six years from item (c). For model in (c), larger slip rates, (brown contours where V > 10 Vpl_{ref}) extend all the way to the trench, whereas in the preferred model only slip rates close to the plate rate (beige contours) reach the trench.

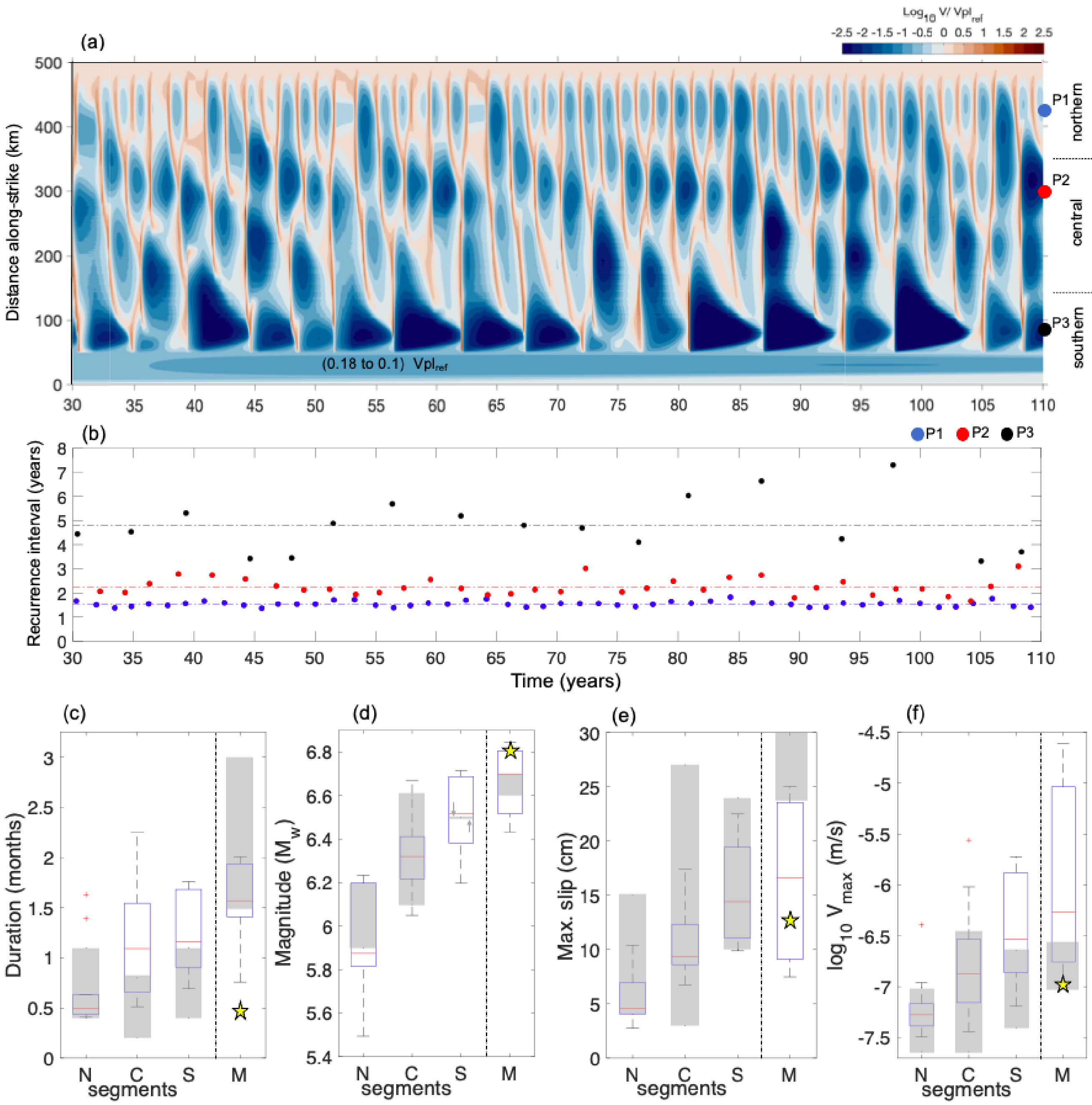

Figure S7. Results for *Model B*. Simulation case with different parametrization in the southern part of the fault (0 km < Y < 50 km) to better model the strongly locked region. (a) Evolution of slip velocity along strike, in $\log_{10}$ (V/Vpl_{ref}) scale, at 10 km depth. The slip rate in the southern part of the margin are in the range of 0.18 to 0.1 Vpl_{ref} after ∼35 years, although the velocity gradually increases over time. (b) Recurrence interval of slow slip episodes at points P1, P2 and P3 (colored circles in item (a), see map view location in Figure 2a). (c-f) Box plot shows the distribution of source properties of modeled SSEs at each segment. N, C, S correspond to northern, central and southern segments. M denotes multisegment SSEs.

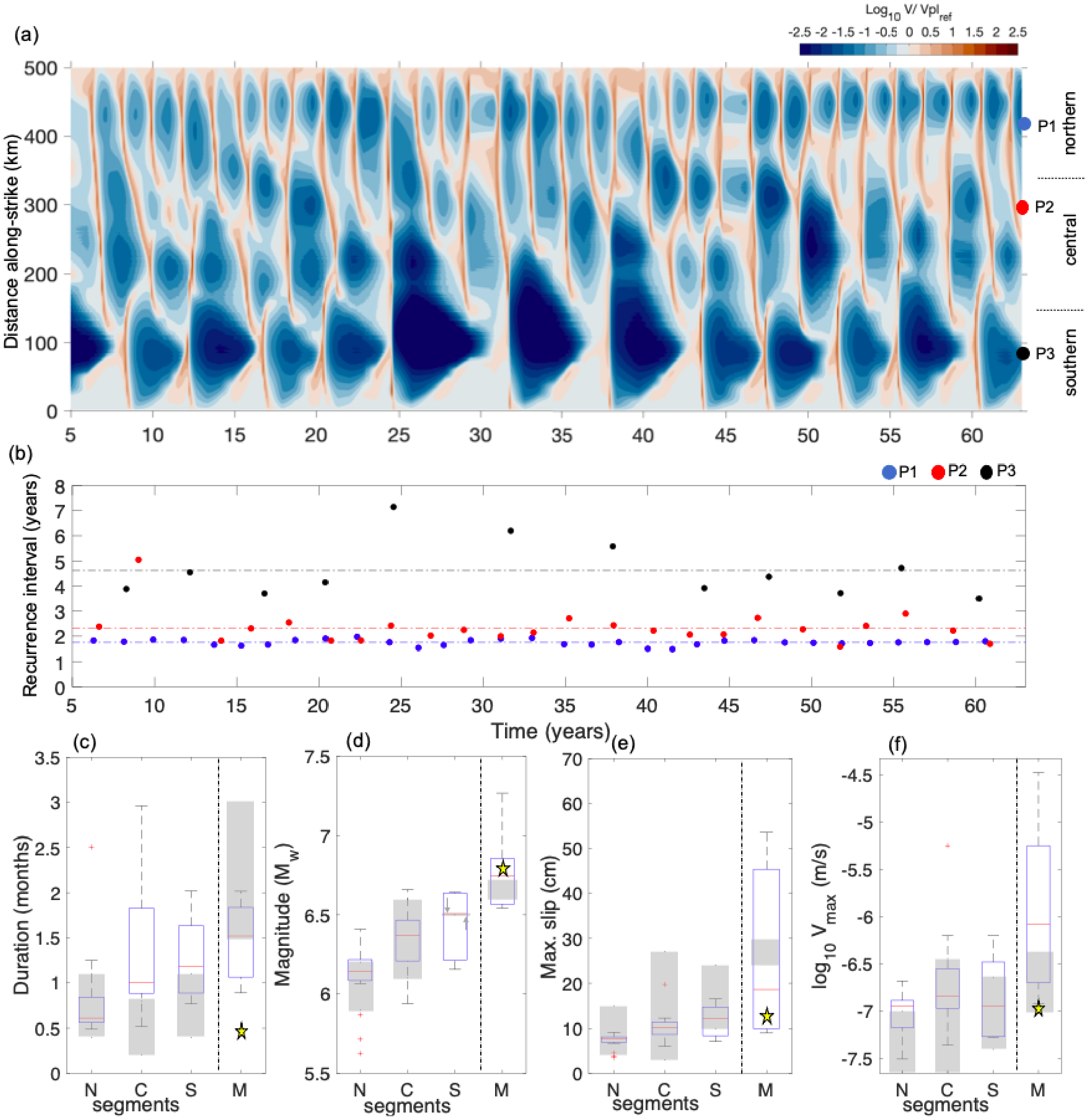

Figure S8. Results for *Model C*. Simulation case without VS and VW bands on the northern and southern ends of the model geometry, respectively. (a) Evolution of slip velocity along strike, in $\log_{10}$ (V/Vpl$_{\mathrm{ref}}$) scale, at 10 km depth. (b) Recurrence interval of slow slip episodes at points P1, P2 and P3 (colored circles in item (a), see map view location in Figure 2a). (c-f) Box plot shows the distribution of source properties of modeled SSEs at each segment. N, C, S correspond to northern, central and southern segments. M denotes multisegment SSEs. Gray bars indicate observed ranges for SSEs' source properties taken from Ikari et al. (2020) catalog. Box plot description is the same as for Figure 6 in the main text.

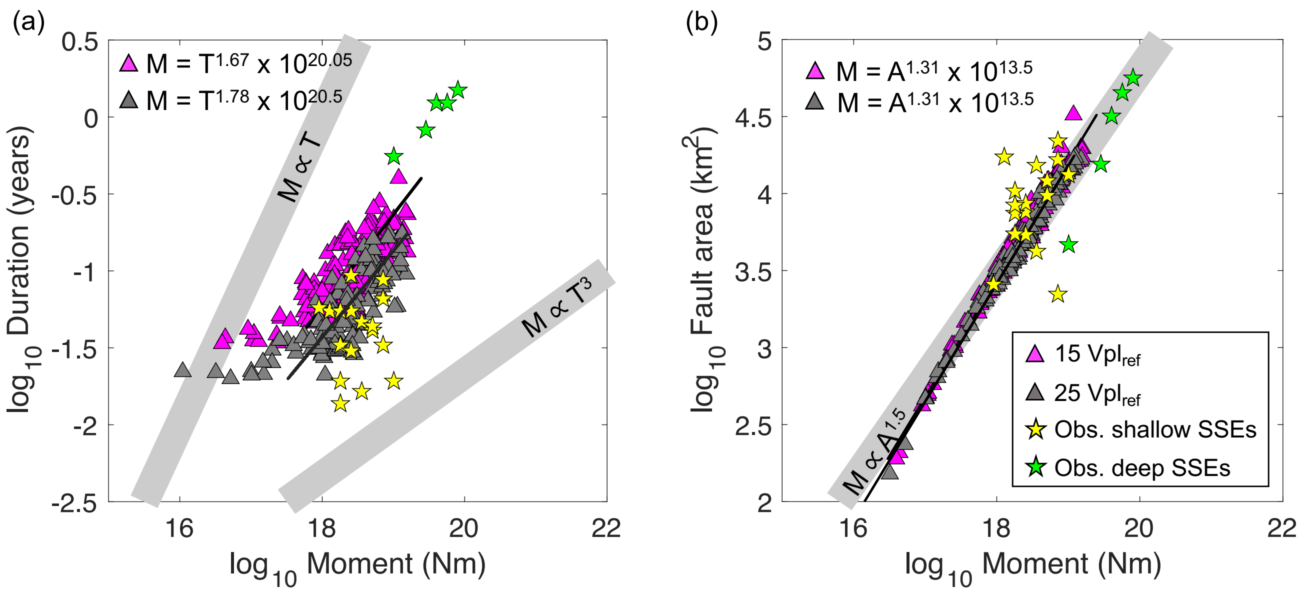

Figure S9. Scaling relations for modeled SSEs (triangles), assuming two different velocity thresholds: 15 Vpl_{ref} or 1.85 mm/day (magenta triangles) and 25 Vpl_{ref} or 3.08 mm/day (gray triangles). Source properties from observed shallow (yellow stars) and deep (green stars) SSEs (taken from Ikari et al. (2020) catalog) are included for comparison. (a) Moment-duration scaling. $M \propto T$ and $M \propto T^3$ scaling are shown as reference. (b) Moment-area scaling. $M \propto A^{1.5}$ is shown as reference. Best fit scaling for simulated SSEs shown as black line and given on top of the figure for each velocity threshold. Results correspond to the preferred model described in the main text.

References

Ampuero, J.-P., & Rubin, A. M. (2008). Earthquake nucleation on rate and state faults–Aging and slip laws. *Journal of Geophysical Research: Solid Earth*, *113*, B01302. doi: 10.1029/2007JB005082.

Bhattacharya, P., Rubin, A. M., & Beeler, N. M. (2017). Does fault strengthening in laboratory rock friction experiments really depend primarily upon time and not slip? *Journal of Geophysical Research: Solid Earth*, *122*(8), 6389–6430. doi: 10.1002/2017JB013936.

Blanpied, M., Marone, C., Lockner, D., Byerlee, J., & King, D. (1998). Quantitative measure of the variation in fault rheology due to fluid-rock interactions. *Journal of Geophysical Research: Solid Earth*, *103*(B5), 9691–9712. doi: 10.1029/98JB00162.

Dieterich, J. H. (1979). Modeling of rock friction: 1. Experimental results and constitutive equations. *Journal of Geophysical Research: Solid Earth*, *84*(B5), 2161–2168. doi: 10.1029/JB084iB05p02161.

Ikari, M. J., Wallace, L. M., Rabinowitz, H. S., Savage, H. M., Hamling, I. J., & Kopf, A. J. (2020). Observations of laboratory and natural slow slip events: Hikurangi subduction zone, New Zealand. *Geochemistry, Geophysics, Geosystems*, *21*(2), e2019GC008717. doi: 10.1029/2019GC008717.

Kaneko, Y., Nielsen, S. B., & Carpenter, B. M. (2016). The onset of laboratory earthquakes explained by nucleating rupture on a rate-and-state fault. *Journal of Geophysical Research: Solid Earth*, *121*(8), 6071–6091. doi: 10.1002/2016JB013143.

Kato, N., & Tullis, T. E. (2001). A composite rate-and state-dependent law for rock friction. *Geophysical Research Letters*, *28*(6), 1103–1106. doi: 10.1029/2000GL012060.

Liu, Y., & Rice, J. R. (2005). Aseismic slip transients emerge spontaneously in three-dimensional rate and state modeling of subduction earthquake sequences. *Journal of Geophysical Research: Solid Earth*, *110*, B08307. doi: 10.1029/2004JB003424

Liu, Y., & Rice, J. R. (2007). Spontaneous and triggered aseismic deformation transients in a subduction fault model. *Journal of Geophysical Research: Solid Earth*, *112*, B09404. doi: 10.1029/2007JB004930.f.

Marone, C., Raleigh, C. B., & Scholz, C. (1990). Frictional behavior and constitutive modeling of simulated fault gouge. *Journal of Geophysical Research: Solid Earth*, *95*(B5), 7007–7025. doi: 10.1029/JB095iB05p07007.

Rice, J. R. (1993). Spatio-temporal complexity of slip on a fault. *Journal of Geophysical Research: Solid Earth*, *98*(B6), 9885–9907. doi: 10.1029/93JB00191.

Rubin, A. M., & Ampuero, J.-P. (2005). Earthquake nucleation on (aging) rate and state faults. *Journal of Geophysical Research: Solid Earth*, *110*, B11312. doi: 10.1029/2005JB003686.

Scholz, C. H. (1998). Earthquakes and friction laws. *Nature*, *391*(6662), 37–42. doi: 10.1038/34097.

Stuart, W. D., Hildenbrand, T. G., & Simpson, R. W. (1997). Stressing of the New Madrid seismic zone by a lower crust detachment fault. *Journal of Geophysical Research: Solid Earth*, *102*(B12), 27623–27633. doi: 10.1029/97JB02716.

Wallace, L. M., & Beavan, J. (2010). Diverse slow slip behavior at the Hikurangi subduction margin, New Zealand. *Journal of Geophysical Research: Solid Earth*, *115*, B12402. doi: 10.1029/2010JB007717.

Wallace, L. M., Beavan, J., McCaffrey, R., & Darby, D. (2004). Subduction zone coupling and tectonic block rotations in the North Island, New Zealand. *Journal of Geophysical Research: Solid Earth*, *109*, B12406. doi: 10.1029/2004JB003241.

Williams, C. A., Eberhart-Phillips, D., Bannister, S., Barker, D. H., Henrys, S., Reyners, M., & Sutherland, R. (2013). Revised interface geometry for the Hikurangi subduction zone, New Zealand. *Seismological Research Letters*, *84*(6), 1066–1073. doi: 10.1785/0220130035.